Acta Materialia 306 (2026) 121880

Contents lists available at ScienceDirect

Acta Materialia

journal homepage: www.elsevier.com/locate/actamat

Effects of twinning configurations on the mechanical performance of small-scale FCC metallic materials

Jinqiao Liu [a,b], Ranming Niu [a,b], Ji Gu [c], Ying Liu [a,b], Song Ni [c], Julie Cairney [a,b], Min Song [c], Yiu-Wing Mai [a], Ting Zhu [d], Xiaozhou Liao [a,b,*]

[a] School of Aerospace, Mechanical and Mechatronic Engineering, The University of Sydney, Sydney, NSW 2006, Australia
[b] Australian Centre for Microscopy & Microanalysis, The University of Sydney, Sydney, NSW 2006, Australia
[c] State Key Laboratory of Powder Metallurgy, Central South University, Changsha 410083, China
[d] Woodruff School of Mechanical Engineering, Georgia Institute of Technology, Atlanta, GA 30332, United States

ARTICLE INFO

Keywords:
Deformation twinning
Mechanical properties
Microstructures
High-entropy alloys
In situ transmission electron microscopy

ABSTRACT

The increasing demand for high-performance miniaturised devices has sparked extensive interest in enhancing the mechanical properties of micro- and nano-sized materials. Deformation twinning, a fundamental mechanism known for enabling strength–ductility synergy in bulk materials, has emerged as a potential strengthening strategy for small-scale systems. However, the relationship between twinning behaviour and the mechanical performance of small-sized materials remains poorly understood. This study employs quantitative in-situ tensile straining transmission electron microscopy combined with comprehensive microstructural characterisation to investigate the effects of three critical aspects of twinning behaviour on mechanical performance in small-sized face-centred cubic metallic materials: twin density, twin–twin interactions, and modes of twin boundary motion. The findings reveal that: (1) increasing twin density improves ductility of small-sized samples, but this effect hinges on the absence of stress-concentration sites; (2) twin–twin interactions, caused by their intersecting behaviour, induce stress concentration and promote necking, resulting in a distinct fracture mechanism compared to single-system twinning; and (3) twin-boundary sliding, in contrast to twin-boundary migration, leads to highly localised deformation, pronounced softening, and significantly reduced ductility. These results provide important insights into the structural design of small-sized single-crystalline materials where twinning-induced plasticity is a dominant deformation mechanism.

1. Introduction

The growing demand for high-performance miniaturised devices in fields such as mechatronic [1], biomedical [2], and aerospace engineering [3] has driven intense interest in understanding the mechanical behaviour of materials at micro- and nano-scales. At these scales, a prominent phenomenon known as the "size effect" has been observed [4–10]. This effect highlights a dependence of mechanical behaviour on specimen dimensions, meaning that materials at small scales can exhibit significantly different properties compared to their bulk counterparts.

Deformation twinning is an important mechanism for accommodating plastic deformation in crystals [11,12]. In face-centred cubic (FCC) materials, deformation twinning occurs when <112>/6 partial dislocations glide across consecutive {111} planes [13,14]. The formation of deformation twins introduces interfaces between the twin domains and the matrix called twin boundaries (TBs). These TBs act as effective dislocation barriers, thereby decreasing the average distance that dislocations travel [15] and increasing the dislocation storage capacity [16], which in turn improves the materials' strength [17,18] and work-hardening capability [19,20]. The enhanced hardening capability extends uniform deformation, thus improving ductility [21–24] and fracture toughness [25–28]. Due to these benefits on the mechanical properties, deformation twinning has become a focal point and a desirable characteristic in the design of structural materials aiming towards outstanding strength and ductility synergy [29].

The excellence of deformation twinning in promoting the mechanical properties of bulk materials has aroused the interest of exploring the possibility of applying the same mechanism to materials in miniaturised

* Corresponding author at: School of Aerospace, Mechanical and Mechatronic Engineering, The University of Sydney, Sydney, NSW 2006, Australia.
E-mail address: xiaozhou.liao@sydney.edu.au (X. Liao).

https://doi.org/10.1016/j.actamat.2025.121880
Received 19 August 2025; Received in revised form 5 December 2025; Accepted 28 December 2025
Available online 30 December 2025

systems [30,31]. However, the size effect precludes a straightforward extrapolation of bulk behaviour to small dimensions, necessitating further investigation into how deformation twinning influences mechanical properties at reduced scales. While most prior studies at small scales have concentrated on the formation and propagation mechanisms of twins [14,32–34], relatively few have comprehensively addressed how different twinning configurations impact the mechanical performance of small-sized materials [35,36].

Three specific aspects of twinning configuration have been identified as key contributors to plastic deformation: (1) twin density, which is determined by twin thickness and TB spacing, (2) the interactions between twins, and (3) the mode of TB motion. The twin density affects the number of interfaces introduced into the material, which in turn influences dislocation blocking and storage capacity [28,37–39]. In addition, twin thickness can impact how dislocations pass through twins, such as by gliding along {111} planes or via unconventional {100} slip [40,41]. Moreover, interactions between twins can create complex internal stress and strain fields, presenting additional obstacles to dislocation motion and fostering intricate defect interactions [42,43]. Meanwhile, the mode of TB motion [44–46], whether through migration or sliding, determines the manner in which plasticity is accommodated [47,48]. Collectively, these factors play a crucial role in dictating the contribution of twinning to mechanical response, particularly at small scales. A comprehensive understanding of these aspects is therefore essential for leveraging twinning to tailor mechanical properties in miniaturised applications.

To adjust the twin density, an effective approach is by tuning the stacking fault energy (SFE) of the material [14,49,50], which in turn can be tailored through compositional modification [51]. In conventional alloys, e.g., Cu-Al alloys [52], where a small number of solute atoms are dissolved in a solvent matrix, lattice distortion is localised around the solute atom sites [53]. As a result, solid solution strengthening in such systems is typically sensitive to the concentration of the solute atoms [53,54]. Consequently, attempts to modify the SFE via compositional tuning in conventional alloys often lead to significant changes to solid solution strengthening, making it challenging to isolate the effects of SFE on mechanical properties from those of solid solution strengthening [49, 53]. In contrast, HEAs, which contain multiple principal elements in near-equiatomic ratios, exhibit severe lattice distortion throughout the crystal lattice [55–57]. As such, we anticipate that this widespread lattice distortion in HEAs attenuates the sensitivity of solid solution strengthening to moderate compositional changes. Leveraging this advantage, two HEAs with the same base elements but different compositions were selected for this study: $Cr_{26}Mn_{20}Fe_{20}Co_{20}Ni_{14}$ and $Cr_{14}Mn_{20}Fe_{20}Co_{20}Ni_{26}$. The SFEs of $Cr_{26}Mn_{20}Fe_{20}Co_{20}Ni_{14}$ and $Cr_{14}Mn_{20}Fe_{20}Co_{20}Ni_{26}$ were initially determined as approximately 3.5 mJ/m^2 and 57.7 mJ/m^2, respectively, by Zaddach et al. using density function theory combined with x-ray diffraction [51]. However, Wagner et al. later argued that this method could yield lower SFE values compared to direct measurements of Shockley partial separations using TEM [58], by which the SFEs of HEA#1 and HEA#2 were re-evaluated, resulting in measurements of 23±3 mJ/m^2 and 69±15 mJ/m^2, respectively. Conversely, Shih et al., through atomistic simulations, proposed that experimental measurements for concentrated alloys might overestimate the SFE due to the neglect of dislocation/solute interaction energy [59]. Despite ongoing discrepancies in the absolute values of the SFEs, the increasing trend from the SFE of $Cr_{26}Mn_{20}Fe_{20}Co_{20}Ni_{14}$ to that of $Cr_{14}Mn_{20}Fe_{20}Co_{20}Ni_{26}$ is widely acknowledged [58–60]. Therefore, they are hereafter referred to as HEA-LSFE and HEA-HSFE, respectively. The different SFEs result in contrasting twinning propensities and consequently distinct twin densities, while the corresponding difference in solid solution strengthening is expected to be minimal.

On the other hand, twin–twin interactions are prone to occur when multiple twinning systems with intersecting planes are simultaneously activated [61,62]. The likelihood of this activation depends strongly on the Schmid factors of twinning systems under the applied loading condition [43,44,63]. Similarly, the mode of TB motion, either TB migration or TB sliding, is governed by the type of partial dislocation activity on the twin plane [44,64], which is also influenced by the Schmid factors of the twinning system [44,65]. By adjusting the alignment between a specific crystallographic orientation of a single crystal and the tensile loading direction, we can regulate the Schmid factors on individual slip systems. This control allows us to manipulate the interaction of twins on different twinning systems as well as to realise different modes of TB motion.

In this study, utilising the aforementioned methodologies, a series of quantitative in-situ tensile straining transmission electron microscopy (TEM) experiments were conducted to explore the roles of twin thickness, twin–twin interactions, and TB motion in small-sized samples.

2. Experimental procedures

2.1. Bulk materials preparation

The $Cr_{26}Mn_{20}Fe_{20}Co_{20}Ni_{14}$ (HEA-LSFE) and $Cr_{14}Mn_{20}Fe_{20}Co_{20}Ni_{26}$ (HEA-HSFE) were fabricated by arc-melting high-purity elemental metals (≥99.99 wt.%) in an argon atmosphere, with titanium used as a gettering agent. Each ingot was re-melted at least four times to ensure chemical homogeneity throughout the bulk material. The ingots then underwent solution treatment at 1473 K for 48 hours within an argon atmosphere. The solution-treated materials were then cold-rolled into 2 mm-thick sheets and subsequently annealed at 1173 K for 2 hours in a vacuum furnace, resulting in an equiaxed coarse-grained microstructure.

2.2. In-situ tensile straining TEM and post-mortem microstructural analysis

Square pieces with dimensions of 10 × 10 × 1 mm^3 were sectioned from the bulk materials using a Struers Accutom-50 diamond saw. These pieces were mechanically ground using silicon carbide abrasive papers with grit sizes of 30 μm, 15 μm, and 5 μm, followed by sequential polishing with a 3 μm diamond suspension and a final step using 0.05 μm colloidal silica. Polishing was continued until the surface was free of visible scratches under an optical microscope.

Dog-bone-shaped samples with gauge dimensions of approximately 1400 nm × 350 nm × 100 nm (length × width × thickness) were prepared for in-situ TEM tensile tests following the procedure below. Grains with a <110> crystallographic orientation normal to the observation plane were first identified via electron backscattered diffraction mapping. From these grains, lamellae measuring 40 μm × 10 μm × 3 μm were extracted using a micro-manipulator integrated into an FEI Helios G4 UXe dual-beam plasma focused ion beam (FIB) scanning electron microscope (SEM). Using a Zeiss Auriga FIB SEM, initial shaping was carried out via rough milling using a 30 kV/100 pA beam, followed by fine thinning and patterning using a 30 kV/50 pA beam. To ensure uniform thickness across the gauge section, a series of pre-thinning trials were conducted to determine the optimal pre-tilt angles for FIB milling. Final cleaning of the sample surfaces was performed sequentially using 10 kV/50 pA and 5 kV/50 pA beams to minimise ion-induced damage [66]. Energy dispersive X-ray spectroscopy was performed to confirm that the real compositions closely matched the nominal values and exhibited a uniform elemental distribution at both micro- and nano-scales.

Fig. 1a presents an SEM image of a single-crystalline tensile sample with the gauge region highlighted. The tensile loading direction was aligned with the gauge section. A Thompson tetrahedron [67] is included to illustrate the crystallographic orientation of the sample, where the edge BC (red) is normal to the observation plane, and the edge AD (blue) is approximately vertical. This configuration enables activation of two {111} slip planes (ABC in green and BCD in purple). The other two {111} planes (ABD and ACD) contain only slip systems with

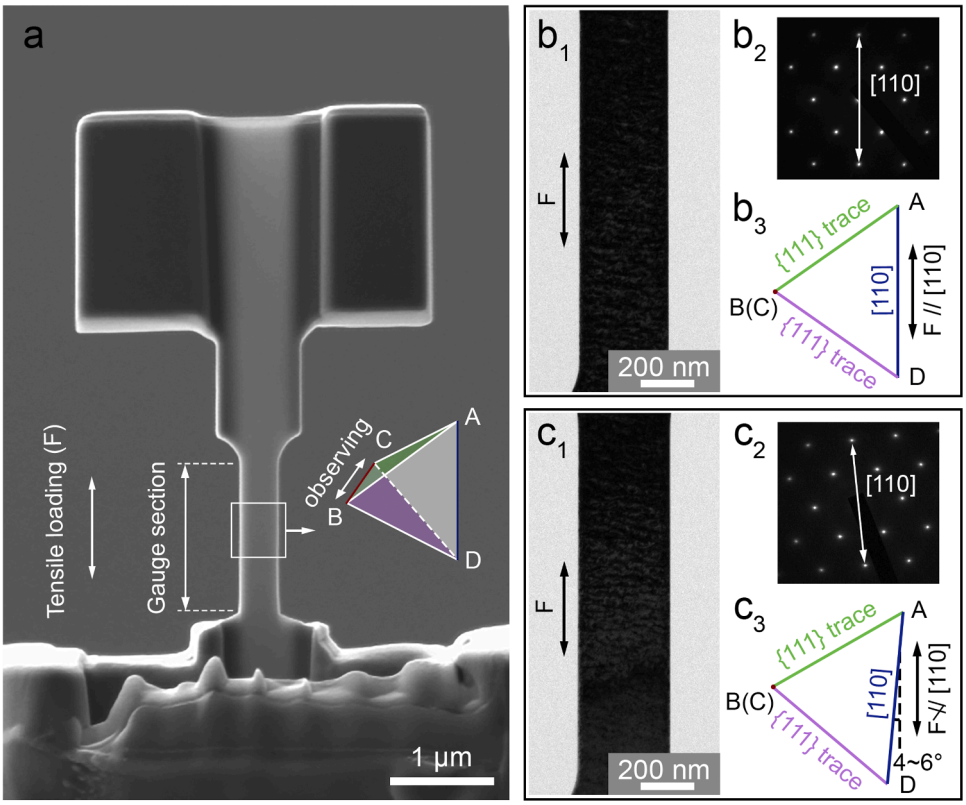

Fig. 1. Geometry and orientation design of in-situ tensile samples. (a) An SEM image of a single-crystalline dog-bone sample, with its gauge section highlighted. The tensile load was along the gauge section. A white square indicates the region whose crystallographic orientation is illustrated using a Thompson tetrahedron. Planes ABC (green) and BCD (purple) represent two {111} slip planes, with the viewing direction oriented along BC. The edge AD was approximately vertical. (b_1–b_3) TEM image of the gauge section (b_1), corresponding SAED pattern (b_2), and the projected Thompson tetrahedron (b_3) for a sample in which the [110] axis (AD) was precisely aligned with the loading direction. (c_1–c_3) Corresponding images for a second sample in which the [110] axis (AD) was intentionally misaligned from the loading direction by 4–6°, resulting in asymmetric activation conditions for the slip and twinning systems.

zero Schmid factors and are thus inactive.

To manipulate the activation of different slip systems, two orientation configurations were designed. In the first configuration (Fig. 1b_1–1b_3), a <110> axis (represented by AD) was precisely aligned with the tensile loading direction. For the convenience of expression, we define this reference <110> direction as the [110] axis. Fig. 1b_1 shows a TEM image of a gauge section, while Fig. 1b_2 displays the corresponding selected-area electron diffraction (SAED) pattern. Double-ended arrows in both images indicate the same orientation for the tensile loading direction and the [110] axis. Fig. 1b_3 shows the projected Thompson tetrahedron from the observating direction, illustrating that the two {111} slip planes (green and purple) are crystallographically equivalent with respect to the loading direction. Crystallographic analysis (Fig. S1 and Table S1) further confirms that the slip systems on these two planes share identical Schmid factors with each other, suggesting equal activation probabilities for dislocation activity on these two planes under this loading condition.

In the second configuration, the [110] axis (AD) was intentionally misaligned by 4–6° from the tensile direction (Fig. 1c_1–1c_3). As shown in Fig. S1 and Table S1, this angular deviation resulted in different Schmid factors for slip systems on different {111} planes, thereby leading to different activation probabilities.

In-situ tensile testing was conducted using a Hysitron PI95 PicoIndenter holder in a JEOL JEM-2100 TEM. The tests were conducted using a displacement-controlled mode at a constant strain rate of 10^{-3} s^{-1}. As small-sized samples usually exhibit a stochastic and anisotropy manner of deformation [68], decorated with frequent strain bursts [69,70], the selection of the displacement-controlled mode allows for a more controlled and more stable deformation process. Tensile loading was applied using a homemade diamond gripper, which was carefully aligned with the sample to ensure on-axis deformation. Post-mortem scanning transmission electron microscopy (STEM) high-angle annular dark-field (HAADF) imaging was carried out in a Titan Themis-Z double aberration-corrected TEM with a semi-convergence angle of 25.1 mrad and a camera length of 115 mm, corresponding to a collection angle of 48–200 mrad.

3. Results

3.1. Mechanical responses of HEAs with different compositions and loading conditions

Fig. 2a–2b and 2c–2d present engineering stress–strain curves for HEA-LSFE and HEA-HSFE samples, respectively. In Fig. 2a and 2c, the [110] crystallographic axis of each sample was precisely aligned with the tensile loading direction, while Fig. 2b and 2d correspond to samples exhibiting a ~4–6° misalignment between the [110] axis and the loading direction. The exact misalignment angles, measured from TEM images and SAED patterns (see Fig. S2), are shown alongside the stress–strain curves in Fig. 2b and 2d. It should be noted that several samples were not strained to fracture in order to preserve them for post-mortem microstructural analysis, as indicated in the corresponding graphs.

All engineering stress–strain curves display intermittent stress responses and immediate post-yield softening, which are typical characteristics of small-scale mechanical testing on single crystals [49,70–72]. These behaviours arise primarily from the small sample dimensions, which allow dislocations to escape readily from the crystal interior

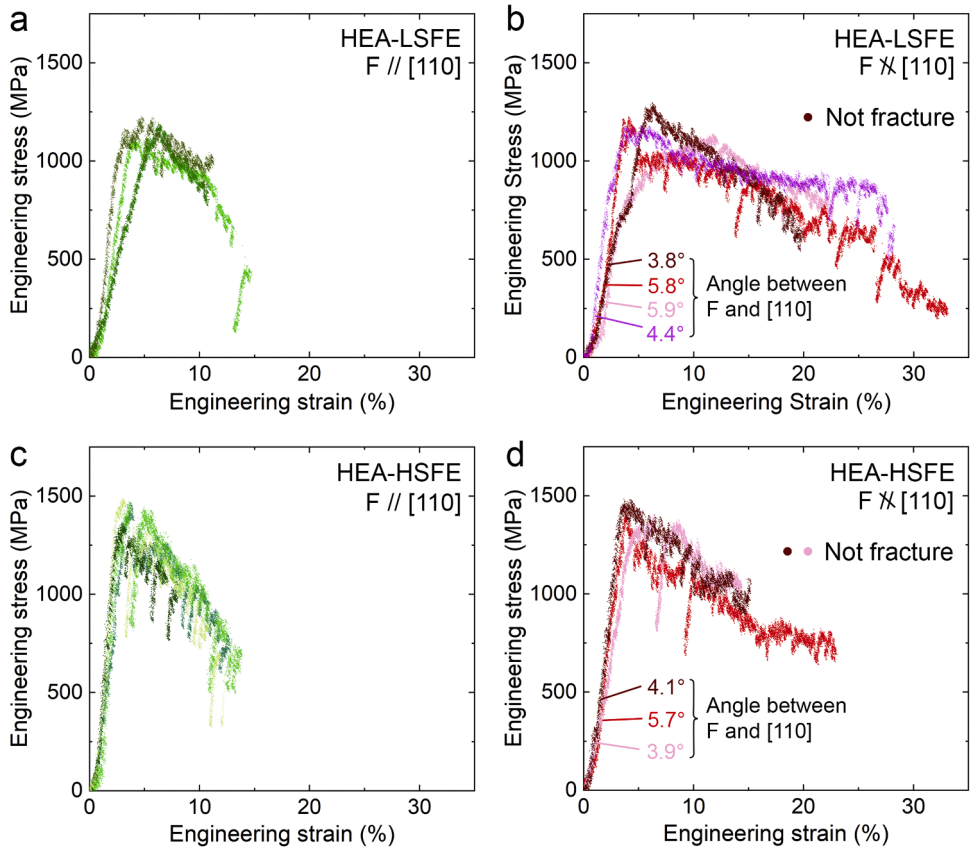

Fig. 2. Typical engineering stress–strain curves for (a–b) HEA-LSFE and (c–d) HEA-HSFE samples under different loading conditions. In (a) and (c), the [110] axis was aligned with the tensile loading direction, whereas (b) and (d) correspond to samples exhibiting a 4–6° misalignment between these two directions. The misalignment angles, measured from TEM/SAED analyses in Fig. S2, are shown alongside the curves.

during deformation [7,73–75]. As a result, the limited dislocation storage capacity suppresses strain hardening and leads to frequent strain bursts throughout deformation [73–75]. Furthermore, some stress–-strain curves exhibit variations in the elastic modulus, arising from the self-alignment and pre-tightening process between the tensile gripper and the sample at the initial stages of loading [76]. This may temporarily cause the tensile axis to deviate from the designed crystallographic direction during the elastic regime. However, once alignment stabilises, the slopes of the re-loading segments after strain bursts become highly consistent, indicating that the plastic deformation follows the intended loading orientation.

A statistical summary of yield strength and ductility for numerous samples is shown in Fig. 3. Red and blue symbols represent HEA-LSFE and HEA-HSFE, respectively, while circles and triangles indicate samples with the [110] axis aligned or misaligned with the loading direction. Open symbols denote samples that were not strained to fracture, indicating that their actual ductility is higher than the plotted values. Most red symbols (representing HEA-LSFE) fall within the yield strength range of 1–1.25 GPa, while most blue symbols (representing HEA-HSFE) lie between 1.25 and 1.5 GPa, indicating that HEA-HSFE generally exhibits higher yield strength than HEA-LSFE. For samples of the same composition, the yield strength remains similar under both loading conditions. Although a slight deviation in loading orientation should, in principle, introduce a small change in yield strength, the corresponding variation in Schmid factor for the most favourably oriented slip system is minimal, increasing only from 0.471 to ~0.493 (Fig. S1 and Table S1). For single crystals, the yield strength, Schmid factor, and critical resolved shear stress are related by

$$\sigma_y = \tau_{CRSS}/m$$

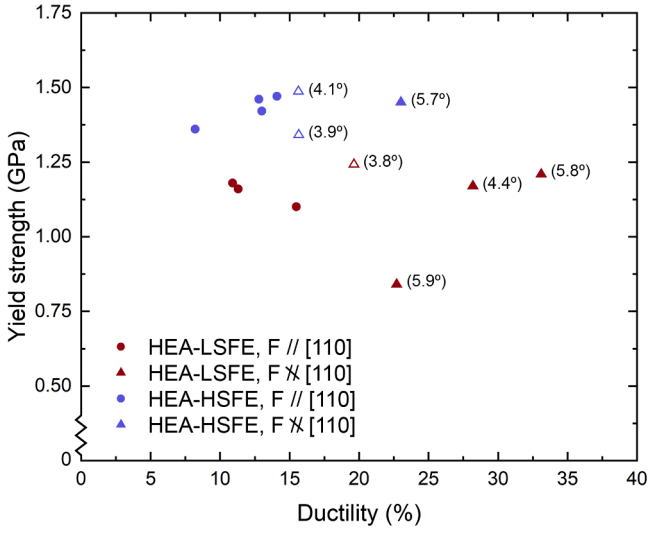

Fig. 3. Statistical analysis of the yield strength and ductility of HEA-LSFE and HEA-HSFE samples under different loading directions. Misalignment angles between the [110] axis and the tensile loading direction are indicated for samples plotted as triangles. Open symbols denote samples that were not strained to fracture.

where σ_y is the yield strength, τ_{CRSS} is the critical resolved shear stress, and m is the Schmid factor [77]. Therefore, assuming the yield strength is σ_y under the aligned [110] loading condition, the corresponding yield strength under a misaligned loading direction would be approximately

$0.96\sigma_y$. Such a small change is easily masked by statistical scatter and therefore does not appear as a noticeable difference in the measured stress–strain curves.

Regarding ductility, all circles (representing perfectly aligned samples) fall within the range of ~7.5–15%, whereas all triangles (representing misaligned samples) exceed 20%. This trend suggests that introducing a misalignment between the [110] crystal orientation and the tensile axis enhances the ductility of the samples. Moreover, although not universal, larger deviation angles often correlate with improved ductility but show no apparent effect on yield strength.

To elucidate the origins of the distinct mechanical responses observed among the different sample categories, the effects of the three previously introduced aspects of deformation twinning, i.e., twin density, twin–twin interaction, and TB motion, are considered and discussed in detail in the following sections.

3.2. *Characterisation of twin density in HEAs with different compositions and loading conditions*

Dark-field (DF) TEM imaging was employed to characterise the deformation twin configurations in the post-deformation samples. Fig. 4a–4d and 4e–4f correspond to HEA-LSFE and HEA-HSFE samples,

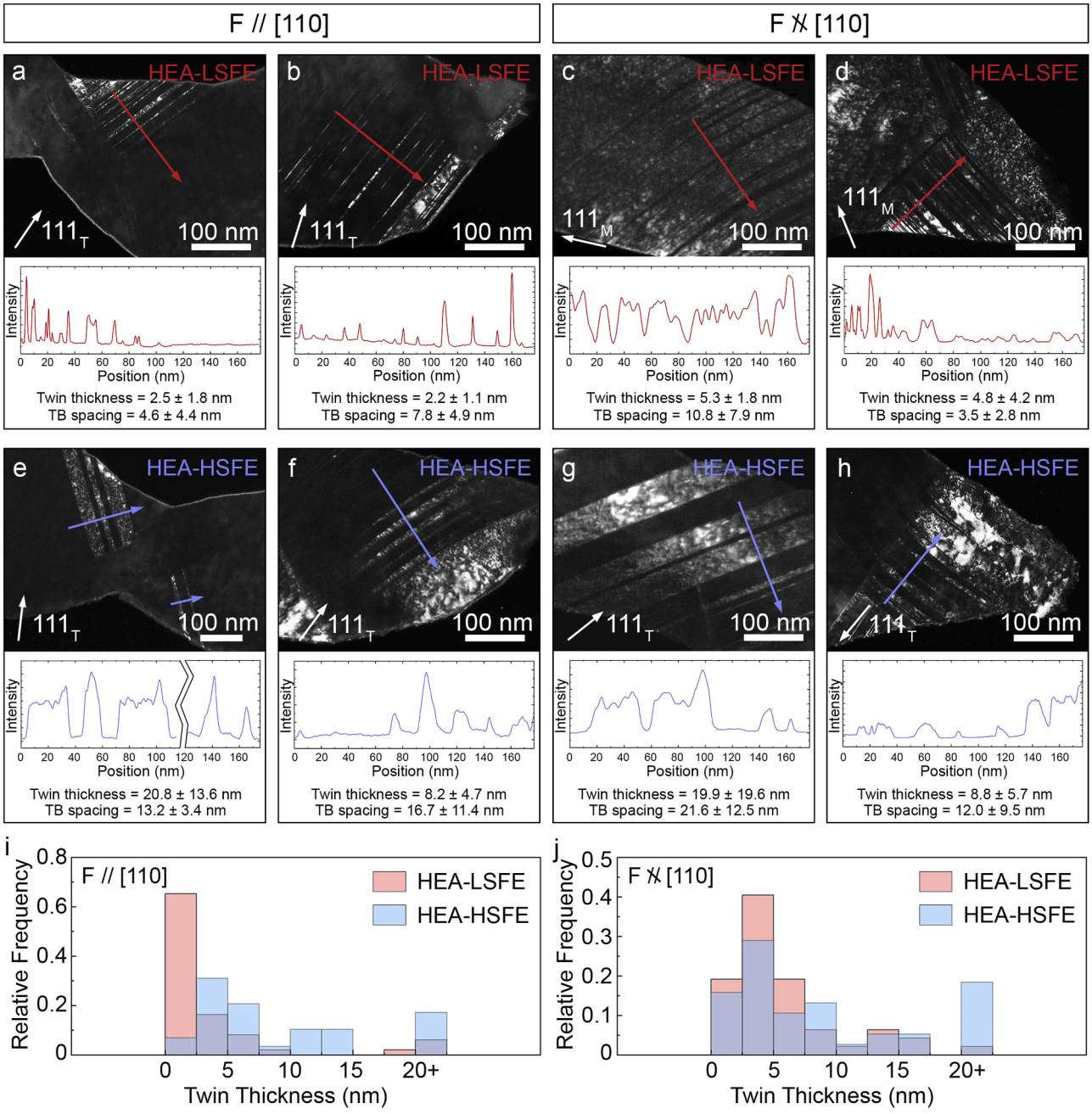

Fig. 4. Dark-field TEM images showing twin configurations in post-deformation (a–d) HEA-LSFE and (e–h) HEA-HSFE samples. In the first two columns, the [110] axis of each sample was aligned with the loading direction, whereas in the latter two columns, the [110] axis was misaligned with the loading direction. White arrows in each image indicate the diffraction spot used to form the DF image, where "T" denotes the twin regions and "M" represents the matrix. Line profiles are extracted along the red or blue arrows to quantify local contrast variations, with the corresponding intensity distributions shown beneath each image. Average twin thicknesses and TB spacings, along with their standard deviations, are measured from the images and intensity profiles. (i–j) Histograms showing twin-thickness distributions in the two alloys under loading directions that are aligned and misaligned with the [110] axis, respectively.

respectively. The first two columns of Fig. 4 show samples in which the tensile loading direction was aligned with the [110] axis, while the third and forth columns present samples where the tensile direction was misaligned from the [110] axis. For each condition, both fractured and unfractured samples were analysed. All DF TEM images were acquired along a <110> zone axis using a 111 diffraction spot of either the twin region or the surrounding matrix. When the 111 spot was taken from the twin region, twin domains appear bright in the resulting DF image; conversely, when the spot was selected from the matrix, the twin domains appear dark.

To quantitatively compare the twin thicknesses and TB spacings between HEA-LSFE and HEA-HSFE, line profiles were drawn across areas exhibiting the highest density of deformation twins, as indicated by red or blue arrows in each image. The corresponding intensity profiles, shown below each DF TEM image, display peaks or valleys associated with individual twins. Average twin thicknesses and TB spacings, along with their standard deviations, were extracted from these intensity profiles. Moreover, Fig. 4i (loading aligned with [110]) and 4j (loading misaligned with [110]) display histograms of twin-thickness distributions, extracted from additional samples with over 150 twins in total. These statistical analysis reveals that deformation twins in HEA-LSFE are generally thinner and denser than those in HEA-HSFE. The findings are consistent with the lower SFE of HEA-LSFE compared to HEA-HSFE [49,50], and align with the experimental design intent of promoting higher twin density in the lower-SFE alloy. Furthermore, the comparison between aligned and misaligned loading conditions indicates that the loading direction has a negligible effect on the twin density.

To further verify these observations, atomic-resolution imaging was conducted using STEM-HAADF. Fig. 5a and 5b display typical twin regions in HEA-LSFE and HEA-HSFE, respectively. In Fig. 5a, the HEA-LSFE sample exhibits a high density of deformation twins, indicated in purple, with the thicknesses of most twin regions being less than 10 atomic layers. The spacings between TBs are usually less than 20 atomic layers. Additionally, stacking faults (SF) (yellow) and a secondary twin (green) are also observed in the HEA-LSFE sample. In contrast, Fig. 5b shows that twins in HEA-HSFE are generally thicker, often on the order of tens of atomic layers, and spaced further apart. Although an ultrathin three-layer twin is observed in Fig. 5b, the overall density of TBs in HEA-HSFE is significantly lower than in HEA-LSFE.

3.3. Deformation behaviour of samples under different loading conditions

3.3.1. [110] aligned with the tensile loading direction

Fig. 3 has shown that samples with a misalignment between the [110] axis and the tensile force direction exhibited greater ductility than those in which the [110] axis was precisely aligned with the loading direction. To gain insight into the underlying mechanisms, the deformation processes of representative samples from each category were examined.

Fig. 6a and 6b present typical engineering stress–strain curves for one HEA-LSFE sample and one HEA-HSFE sample, respectively, both having the [110] axis precisely aligned with the tensile direction. Sequential frames extracted from the corresponding in-situ deformation videos (Supplementary Movies 1 and 2) are shown in Fig. 6c_1–6c_5 and 6d_1–6d_5, with each frame's time point marked on the stress–strain curve.

Because these samples were loaded precisely along the [110] direction, two primary {111} slip plane groups (green and purple planes in Fig. 1b_3) were symmetrically oriented relative to the loading direction and thus activated concurrently during deformation. As highlighted by the red and blue arrows in Fig. 6c_1–6c_2 and 6d_1–6d_2, twins nucleated almost simultaneously on both planes at early stages of deformation and quickly intersected. The moderate twin thickness at this stage facilitated interaction and mutual penetration between intersecting twins, forming X-shaped configurations. In Fig. 6c_2 and 6d_2, the intersected twins are highlighted by blue (T_1 and T_3) and red (T_2 and T_4) dashed lines. The matrix region between these twins are outlined by yellow dashed lines and marked with an “M”. This process resulted in noticeable changes to the sample morphology. Prior to twin intersection, single-step ledges appeared along the sample edges (highlighted by polylines in Fig. 6c_1 and 6d_1). Following the interpenetration, opposing double-step features developed at the edges (Fig. 6c_2–6c_3 and 6d_2–6d_3), separated by a narrow marix region.

With continued deformation, both intersected twins underwent thickening via TB migration, which significantly consumed the matrix region between them. This can be clearly seen by comparing Fig. 6c_2 and 6d_2 with Fig. 6c_4 and 6d_4, respectively, where a pronounced reduction in the matrix area (highlighted by yellow dashed lines) is evident. This processes resulted in a marked decrease in the local cross-sectional area at the intersected-twin region, forming a necked region. As a result, subsequent deformation became increasingly localised at the twin–twin intersection. Once necking became severe, abrupt fracture occurred at that site (Fig. 6c_5 and 6d_5). Moreover, throughout the deformation process, in-situ observations confirmed that TB migration was the dominant mechanism of TB motion, whereas TB sliding was not observed.

3.3.2. [110] misaligned with the tensile loading direction

Fig. 7a and 7b show typical engineering stress–strain curves of HEA-LSFE and HEA-HSFE samples, respectively, in which a misalignment existed between the [110] axis and the tensile loading direction. Both curves exhibit ductility in the range of approximately 20–25%, clearly

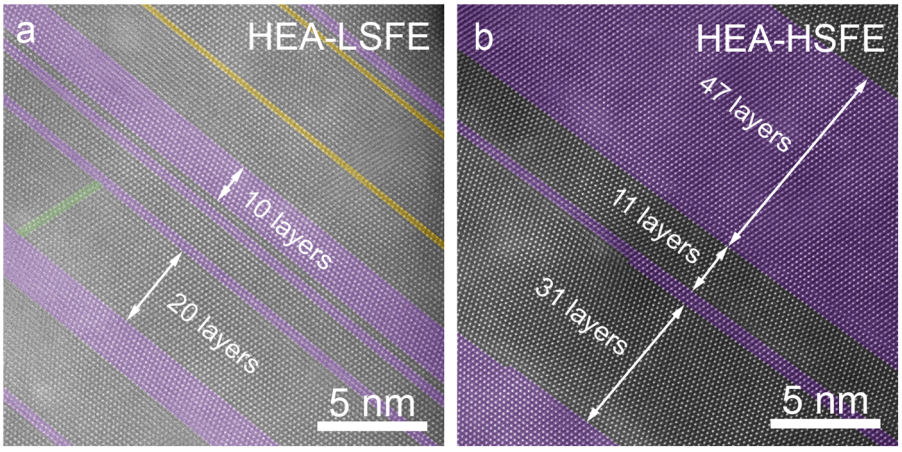

Fig. 5. STEM–HAADF images of post-deformation (a) HEA-LSFE and (b) HEA-HSFE samples showing atomic-scale twin configurations. Uncoloured, purple, green, and yellow areas represent the matrix, primary twins, secondary twins, and SFs, respectively.

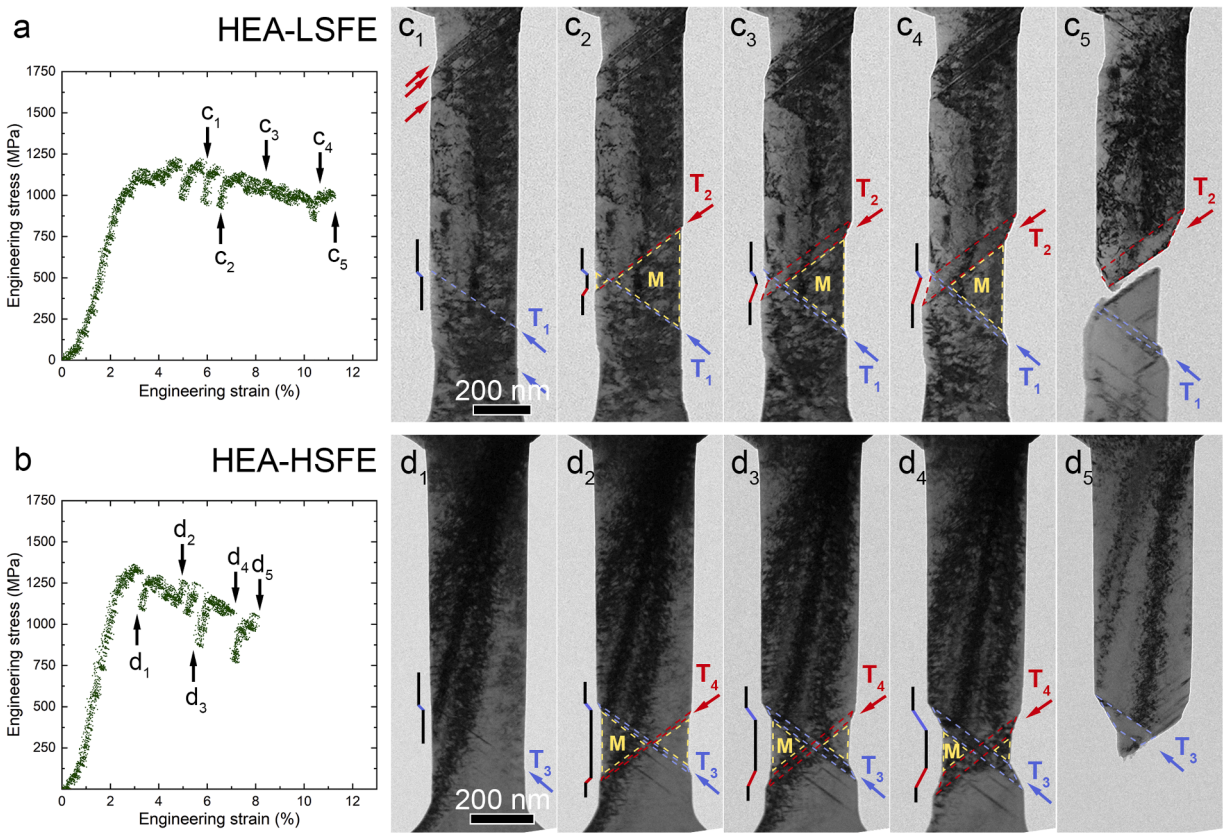

Fig. 6. Deformation processes of samples with the [110] axis precisely aligned with the tensile loading direction. (a–b) Engineering stress–strain curves of representative HEA-LSFE and HEA-HSFE samples, respectively. (c_1–c_5) and (d_1–d_5) Sequential frames extracted from the corresponding in-situ deformation videos of the HEA-LSFE and HEA-HSFE samples, respectively. The time points of each frame are indicated on the stress–strain curves. Red and blue arrows indicate deformation twins formed on two different {111} slip planes. Red/blue and yellow dashed lines highlight intersected twins and the matrix, respectively. Polylines adjacent to the samples outline surface morphologies, where black segments denote matrix regions and red/blue segments represent twinning regions along different directions.

higher than that of the samples shown in Fig. 6.

Fig. 7c_1–7c_5 and 7d_1–7d_5 illustrate the corresponding deformation processes for the two samples, with their in-situ videos shown in Supplementary Movies 3 and 4. Due to the misalignment between [110] and the loading direction, different Schmid factors were realised for slip systems on the two {111} slip plane groups. As a result, deformation twinning in these samples showed a strong directional preference, with most twins forming along a single {111} plane group. As shown in Fig. 7c_1–7c_2 and 7d_1–7d_2, the majority of twins were aligned along the same direction, which significantly reduced interaction between differently oriented twinning systems. In the absence of twin–twin intersections, which are common sites of stress concentration, strain was more uniformly distributed across the samples. This is evidenced by the even dispersion of massive twins and the absence of sharp surface steps at necking regions, as outlined by the black lines in Fig. 7c_3 and 7d_3. The reduction in cross-sectional area was therefore shared across multiple locations, rather than being concentrated at a single site, which contributed to the enhanced ductility.

A notable deformation feature observed in both samples was the bending of individual twin segments, as evidenced by the morphologies of T_1 in Fig. 7c_3 (outlined by blue dashed lines) and T_3 in Fig. 7d_3 (outlined by red dashed lines). The bending of twins is usually caused by the accumulation of full or partial dislocations at TBs [78]. In this case, the gliding of partial dislocations on the less favoured slip planes gave rise to T_2 and T_4 that intersected with the dominant twins T_1 and T_3, forming junctions at points A and B in Fig. 7c_3 and 7d_3, respectively. This leads to accumulation of full or partial dislocations at TBs, causing the bending of T_1 and T_3. These bent twin regions became the sites of localised necking and, eventually, fracture occurred within these regions (Fig. 7c_5 and 7d_5).

3.3.3. *Statistics on twin–twin intersection behaviour*

To further substantiate the role of twin–twin intersections in governing deformation, we performed a statistical analysis of intersection events for HEA-LSFE (Fig. 8a, b) and HEA-HSFE (Fig. 8c, d). These measurements were derived from in-situ tensile videos acquired using diffraction contrast at relatively low magnifications. While this imaging condition may lead to a small number of ultrathin twins being missed, the observable twins, which represent the main carriers of plastic deformation, still provide a reliable semi-quantitative basis for evaluating deformation behaviour.

Fig. 8a and 8c summarise the number of deformation twins activated on different twinning planes at the moment of the first twin–twin intersection. As illustrated by the Thompson tetrahedron in the inset, the blue and purple regions correspond to twins lying on the ABC and BCD twinning planes, respectively. For both HEAs, when the loading direction was aligned with the [110] axis, comparable numbers of twins were activated on both planes. In contrast, when the loading direction was misaligned with the [110] axis, a disproportionately large number of twins formed on one twinning plane, and the overall number of activated twins increased.

Fig. 8b and 8d show the fractions of intersected (light brown) and non-intersected (dark brown) twins among all twins just before fracture. For both HEAs, aligned loading conditions resulted in a dominant fraction of intersected twins. Conversely, under misaligned loading, the proportions of intersected and non-intersected twins became comparable. This behaviour arises because, at early deformation stages, most twins nucleate on the favoured twinning plane, whereas at later stages,

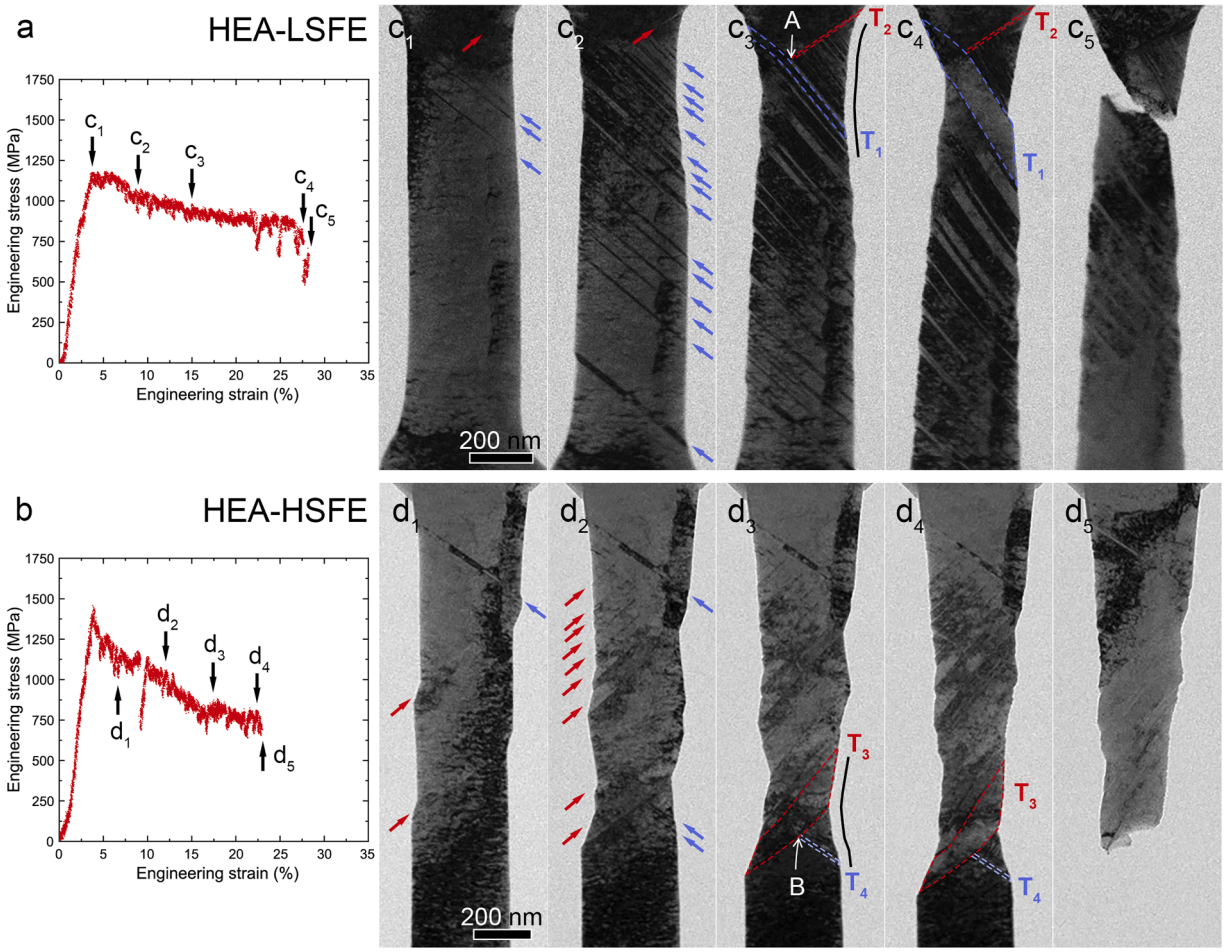

Fig. 7. Deformation processes of samples with misalignment between the <110> axis and the tensile force. (a–b) Engineering stress–strain curves of a representative HEA-LSFE and HEA-HSFE sample, respectively. (c_1–c_5) and (d_1–d_5) Sequential frames extracted from the corresponding in-situ deformation videos of the HEA-LSFE and HEA-HSFE samples, respectively. The time points of each frame are indicated on the stress–strain curves. Red and blue arrows indicate deformation twins formed on two different {111} slip planes. Black lines adjacent to the samples outline surface morphologies. Red and blue dashed lines in (c_3–c_4) and (d_3–d_4) outline representative twins on each direction in each sample, with Point A and B highlighting locations of twin–twin intersection.

the less-favoured plane becomes activated, leading to the formation of twin–twin intersections.

These statistical results confirm that distinct loading conditions give rise to different dynamic twinning behaviours, which in turn underpin the contrasting mechanical responses of the samples.

3.4. *Fracture surfaces of samples under different loading conditions*

To further investigate the fracture mechanisms of the samples and understand the role of twin–twin interactions, the fracture surfaces were examined. Fig. 9a shows the morphology of a sample just before fracture, which was subjected to tensile loading precisely along the [110] axis. Two twins (T_1 and T_2, outlined by red and blue dashed lines, respectively) are clearly seen to interpenetrate. The SAED pattern in the inset confirms the presence of twins on two {111} plane groups. This configuration significantly reduced the local cross-sectional area at the interaction site, increasing the local shear stress and therefore leading to pronounced strain localisation. More importantly, three distinct crystallographic orientations coexisted within the necked region, namely, the matrix (yellow), T_1 (red), and T_2 (blue). The presence of multiple orientations created a complex stress state and increased the likelihood of strain incompatibility. Fig. 9b presents the fracture surface of the same sample. Fracture occurred at the site of twin–twin interpenetration, displaying a relatively flat fracture surface along a TB of T_1 and cutting across T_2. The red dashed lines indicated the original location of T_1, and the blue dashed lines mark the residual part of T_2. A small fragment (highlighted by a white dashed square) is visible on the other side of T_2, corresponding to the yellow dashed triangle in Fig. 9a. This region is further magnified in Fig. 9c, where numerous nanotwins and SFs along different directions are observed, as indicated by the blue and red arrows. This indicates high stress concentration in this area.

Fig. 9d shows the morphology of a sample deformed under a loading direction misaligned with its [110] axis. In this case, most twins were aligned along the same direction, thus avoiding the severe necking caused by twin–twin interpenetration. Instead, necking in this sample was primarily driven by the repeated nucleation of twins. As a result, necking was distributed over a much larger portion of the sample, as highlighted in Fig. 9d. Fig. 9e shows the fracture surface of this sample, where fracture occurred within the bent twin T_3, resulting in an irregular surface approximately perpendicular to the loading direction. Notably, a gradual change in the inclination angle of TBs is observed, from 45° at TB-1 to 62° at TB-4, as marked by white dashed lines. This progressive variation indicates that crystal rotation occurred during deformation.

From the analysis of fracture surfaces under different loading conditions, it can be concluded that fracture typically initiates at locations where twins from different systems intersect or interact. However, the fracture mechanisms differ markedly between the two scenarios. In the first case where two twinning systems are simultaneously activated, the interpenetration of twins results in localised reduction in cross-sectional

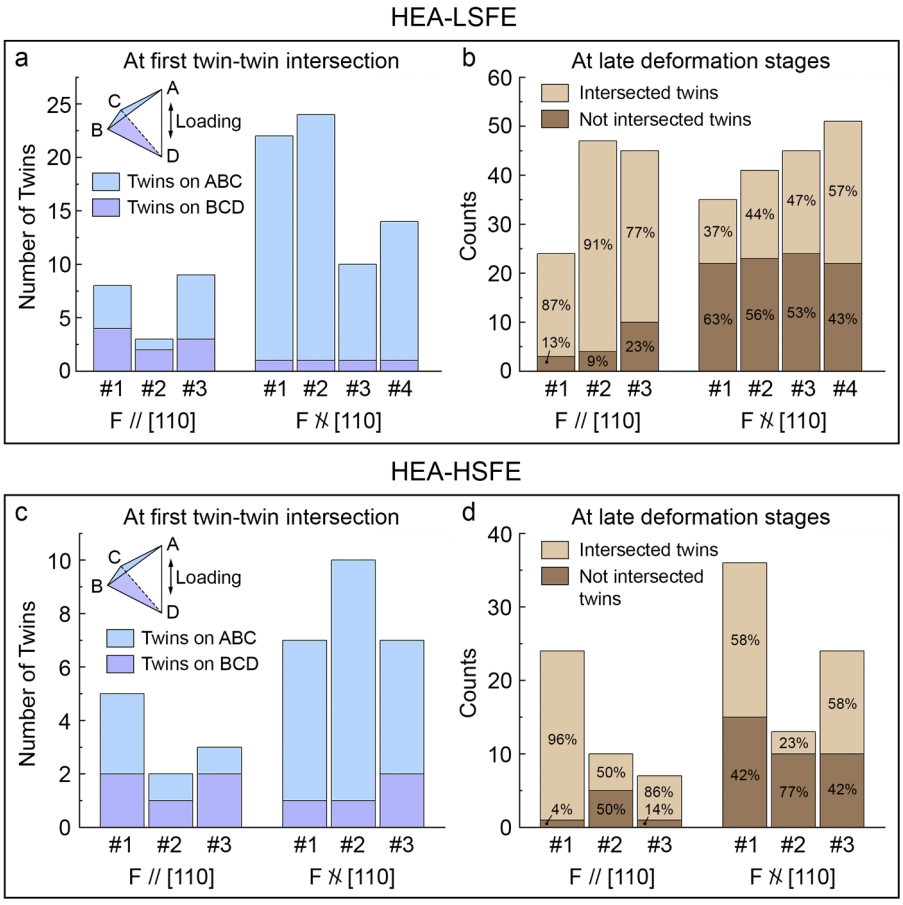

Fig. 8. Statistics of twin–twin intersection events in (a–b) HEA-LSFE and (c–d) HEA-HSFE samples under different loading conditions. (a) and (c) show the number of activated twins on different twinning planes at the moment when the first twin–twin intersection occurred. (b) and (d) show the fractions of intersected and non-intersected twins among all twins just prior to fracture. At least three samples were examined for each loading condition, labelled #1 to #4.

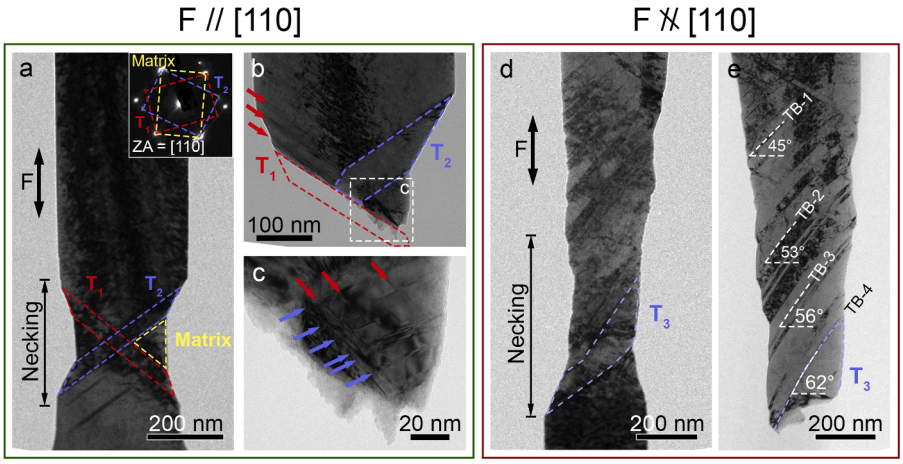

Fig. 9. Fracture mechanisms of post-deformation samples. (a) Morphology of a sample subjected to a tensile loading direction parallel to the [110] axis. Red and blue dashed lines outline two intersecting twins, T_1 and T_2. The yellow dashed lines mark the matrix. The loading direction and necking region are highlighted. The inset displays a <110> SAED pattern, with yellow, red, and blue rectangles marking diffraction spots from the matrix, T_1, and T_2, respectively. (b) Fracture surface of the same sample shown in (a). The red dashed lines indicate the original location of T_1, and the blue dashed lines mark the residual part of T_2. Red arrows indicate twins parallel to T_1. (c) Magnified view of the region highlighted by the white square in (b). Nanotwins/SFs along different directions are indicated by red and blue arrows. (d) Morphology of a sample loaded with a tensile loading direction misaligned from the [110] axis. The loading direction and necking region are marked. The blue dashed lines highlight a bent twin (T_3) and the red arrow points to a twin on a less-favoured plane. (e) Fracture surface of the sample shown in (d), with T_3 outlined by blue dashed lines. White dashed lines indicate four TBs and their corresponding inclination angles.

area, forming a necked region composed of multiple subdomains with different crystallographic orientations. This leads to inter-twin fracture, typically along one of the TBs. In contrast, in the second scenario where only one twinning system is active at early stages of deformation, the

frequent nucleation of twins helps alleviate strain localisation and distribute plastic deformation across a larger region. Fracture usually occurs after another slip plane is activated at a later deformation stage. The accumulation of dislocations on TBs distorts or bends an existing twin, leading to complex stress states and ultimately intra-twin fracture. This mechanism also accounts for the observation that larger misalignment angles between the [110] axis and the loading direction often enhance ductility: such loading conditions reduce the Schmid factors of slip systems on the less-favoured slip planes, thereby delaying their activation and postponing the twin–twin–intersection-induced stress concentration.

3.5. Mechanical behaviour of samples dominated by different modes of TB motion

The experimental results presented so far have primarily focused on samples where TB migration was the dominant mode of TB motion. In fact, TB sliding is an equally important mechanism that occurs when the loading orientation results in comparable Schmid factors for leading and trailing partial dislocations on the slip plane [44].

Fig. 10a presents typical engineering stress–strain curves of HEA-LSFE samples that exhibited pronounced TB sliding during deformation (plotted in blue), which can be confirmed in Supplementary Movies 5–7. For comparison, the curve of a HEA-LSFE sample displaying only TB migration is also shown (in red), with the corresponding in-situ video presented in Supplementary Movie 8. All samples were subjected to tensile loading misaligned from the [110] axis. Compared to the sample dominated by TB migration, the TB-sliding-dominated samples exhibited lower ductility and were characterised by at least one prominent strain burst. Following the strain burst, the flow stress dropped to a significantly lower level and then rapidly declined to zero. In contrast, the TB migration samples showed a more continuous plastic flow and a gradual decrease in stress, thereby better maintaining its ductility.

Fig. 10b summaries the contribution of TB sliding to the overall deformation for the samples shown in Fig. 10a. The fractions of TB-sliding-induced strain relative to the total strain are evaluated at engineering strains of 0.05, 0.10, 0.15, and 0.20. For samples dominated by TB migration, TB sliding remains negligible and emerges only at very late deformation stages. In contrast, TB-sliding-dominated samples exhibit substantially higher TB-sliding contributions, even during the early stages of deformation. As the total strain increases, TB sliding becomes increasingly dominant, ultimately accounting for more than 50% of the total strain at later stages.

Fig. 11a and 11b_1–11b_4 illustrate the deformation process of a HEA-LSFE sample dominated by TB sliding (tensile loading direction misaligned with the [110] axis). The original in-situ video shown in the Supplementary Movie 5. The corresponding time points of each frame (Fig. 11b_1–11b_4) are indicated on the stress–strain curve in Fig. 11a. At early stages of deformation, two twins (T_1 and T_2) nucleated on the same set of {111} planes, as indicated by the blue arrows in Fig. 11b_1. The surface steps at these two twins caused stress concentration and facilitated the nucleation of massive dislocations. As a result, subsequent deformation was mainly localised to these twins through TB sliding, particularly in T_2. As TB sliding proceeded, a large surface step formed on the specimen, as marked by the gap between the red dashed and solid lines in Fig. 11b_2. In Fig. 11b_3, both T_1 and T_2 underwent abrupt TB sliding. Simultaneously, a new twin (T_3) nucleated and also experienced significant TB sliding. This sudden twin formation and collective TB sliding event resulted in a large strain burst at point b_3 on the stress–-strain curve and caused temporary detachment between the tensile gripper and the sample. An unloading adjustment was then performed before reapplying the tensile load. During reloading, a much lower engineering stress was sufficient to continue deformation, as the prior TB sliding had effectively reduced the cross-sectional area of the sample. As deformation progressed, T_3 underwent extensive TB sliding (Fig. 11b_4), ultimately becoming the site of fracture.

The red-rectangle region in Fig. 11b_4 was examined using DF TEM after tensile testing, and the result is shown in Fig. 11c. The inset displays a <110> SAED pattern of the region, with 111 diffraction spots of the matrix and twins highlighted by white and blue circles, respectively. The DF TEM image was obtained using the 111 diffraction beam of the matrix, rendering the twins as dark contrast bands. The thin, dark feature marked by the arrow at T_3 confirms that the observed deformation was due to TB sliding rather than a dislocation slip band.

4. Discussion

4.1. Effects of twin thickness on mechanical behaviour

By varying the composition and consequently the SFE, distinct twin densities were achieved in HEA-LSFE and HEA-HSFE. Specifically, HEA-LSFE, with its lower SFE, exhibited thinner and denser deformation twins compared to HEA-HSFE. This difference primarily stems from the influence of SFE on the nucleation of twin embryos and their subsequent growth [33,50,79].

Mechanically, HEA-HSFE samples exhibited an average yield strength approximately 300 MPa higher than that of HEA-LSFE samples. This difference is more likely attributed to composition-induced variations in SFE and local chemical heterogeneity rather than differences in twin density. Prior studies have shown that increasing Cr content lowers the unstable SFE, whereas increasing Ni content raises it [80,81]. A lower unstable SFE reduces the stress required to nucleate partial

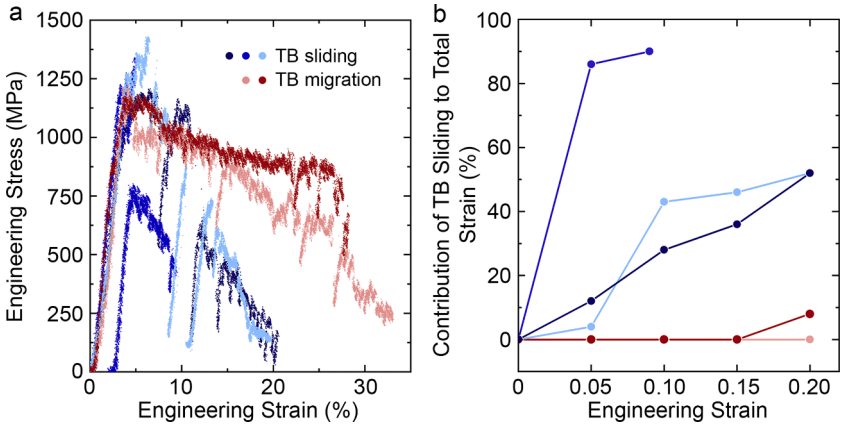

Fig. 10. Comparison of TB-sliding- and TB-migration-dominated mechanical behaviours. (a) Representative engineering stress–strain curves of three TB-sliding-dominated HEA-LSFE samples (blue) and two TB-migration-dominated HEA-LSFE samples (red). (b) Contribution of TB sliding to the total strain for the samples shown in (a).

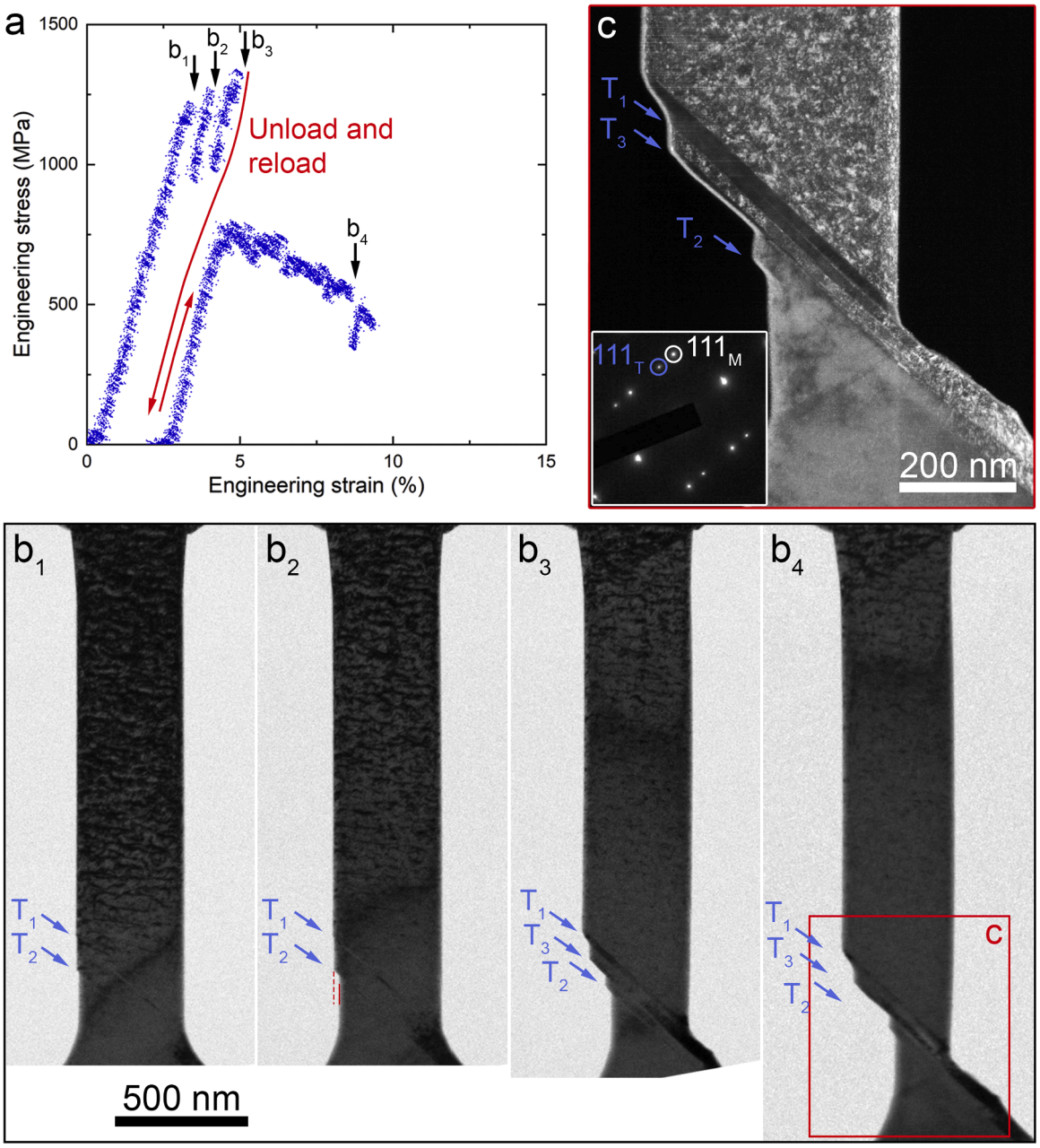

Fig. 11. A TB-sliding-dominated deformation process for a HEA-LSFE sample. (a) The engineering stress–strain curve. (b_1–b_4) Sequential frames from the in-situ deformation video showing the deformation process. Time points of each frame are indicated on the stress–strain curve. Blue arrows highlight deformation twins, T_1, T_2, and T_3. The red dash and red solid lines in (b_2) mark a step formed from TB sliding. The red-square area in (b_4) is observed with DF TEM and shown in (c). The inset in (c) presents the SAED pattern. The 111 diffraction spots of the matrix and twins are highlighted.

dislocations and thus lowers the yield strength [80,82]. In addition, local chemical heterogeneity, including local compositional fluctuations and short-range ordering (SRO), may further contribute to the strength difference. Such heterogeneity is known to generate a rugged energy landscape that impedes dislocation glide [83] and increases the activation energy required for nanoscale segment detrapping, thereby strengthening the alloy [84]. Although all samples in this study were annealed at an elevated temperature for an extended period (see Experimental Procedures) and TEM/STEM characterisation did not reveal measurable differences in these features, it remains possible that the compositional differences between the two HEAs give rise to distinct degrees of local chemical heterogeneity [85]. However, how variations in Cr and Ni concentrations quantitatively influence local compositional fluctuations or SRO remains insufficiently explored and represents a promising direction for future research.

The influence of twin density on ductility, however, depends strongly on the loading condition. When the [110] axis was misaligned with the loading direction, HEA-LSFE samples exhibited slightly higher average ductility (~26%) than HEA-HSFE (~21%). This suggests that increasing twin density can improve the ductility of small-sized samples, consistent with observations in many bulk materials [86–88]. One reason is that a higher density of TBs can increase dislocation storage capacity and postpone the onset of necking [89–92]. Moreover, our observations of structural evolution during deformation (Fig. 7) show that samples with higher twin density developed smoother surface morphologies with less pronounced surface steps at the necking region, thereby alleviating strain localisation and further supporting improved ductility. However, it is important to note that increasing twin density

does not lead to unlimited improvement in ductility. Some studies suggest the existence of a material-specific critical twin thickness [93,94]. When the twin thickness falls below this threshold, an inverse Hall–Petch relationship may be activated, resulting in reduced strength and strain hardening capacity [93,94].

In contrast, when the [110] axis was aligned with the loading direction, both HEAs showed a similar average ductility of ~12%. In this case, increasing twin density did not improve ductility as it did under the previous condition. Our analysis indicates that this is due to frequent twin–twin interactions such as interpenetration, which promote early necking. The increase in TBs could not delay necking, and as a result, both alloys, regardless of their twin densities, exhibited comparably low ductility. More detailed discussion on how twin–twin interactions promote necking and compromise ductility is provided in the following section. Furthermore, these findings lead to an important insight: in small-sized samples, improving ductility is less about increasing dislocation storage capacity and strain hardening capability, as is typical in bulk materials, and more about avoiding the formation of stress concentration sites. Morphological stability and the suppression of localisation are key to enhancing ductility in these systems.

4.2. *Effect of twin–twin interaction on mechanical behaviour*

By adjusting the alignment between the tensile loading direction and the crystal's [110] axis, two distinct deformation scenarios were observed: activation of deformation twinning on either two different sets of {111} plane groups or predominantly on a single set. In the first scenario, twins form along different directions and frequently interact, whereas in the second, twins primarily align along the same direction. In-situ tensile testing and TEM characterisation demonstrate that twin–twin interactions adversely affect the ductility of small-sized single-crystalline samples mainly by promoting localised strain and necking. This behaviour contrasts with that of bulk materials, where twin–twin interactions are generally regarded as beneficial, often enhancing mechanical properties [42,95,96]. For instance, in bulk twinning-induced plasticity steels, twin–twin interactions have been shown to provide additional hardening at late deformation stages, thereby delaying the onset of unstable plastic flow [95]. Twin intersections have also been observed to retard twin growth and promote the nucleation of new twins in their vicinity, both of which contribute to twinning-induced hardening [42,96]. To better understand the reasons

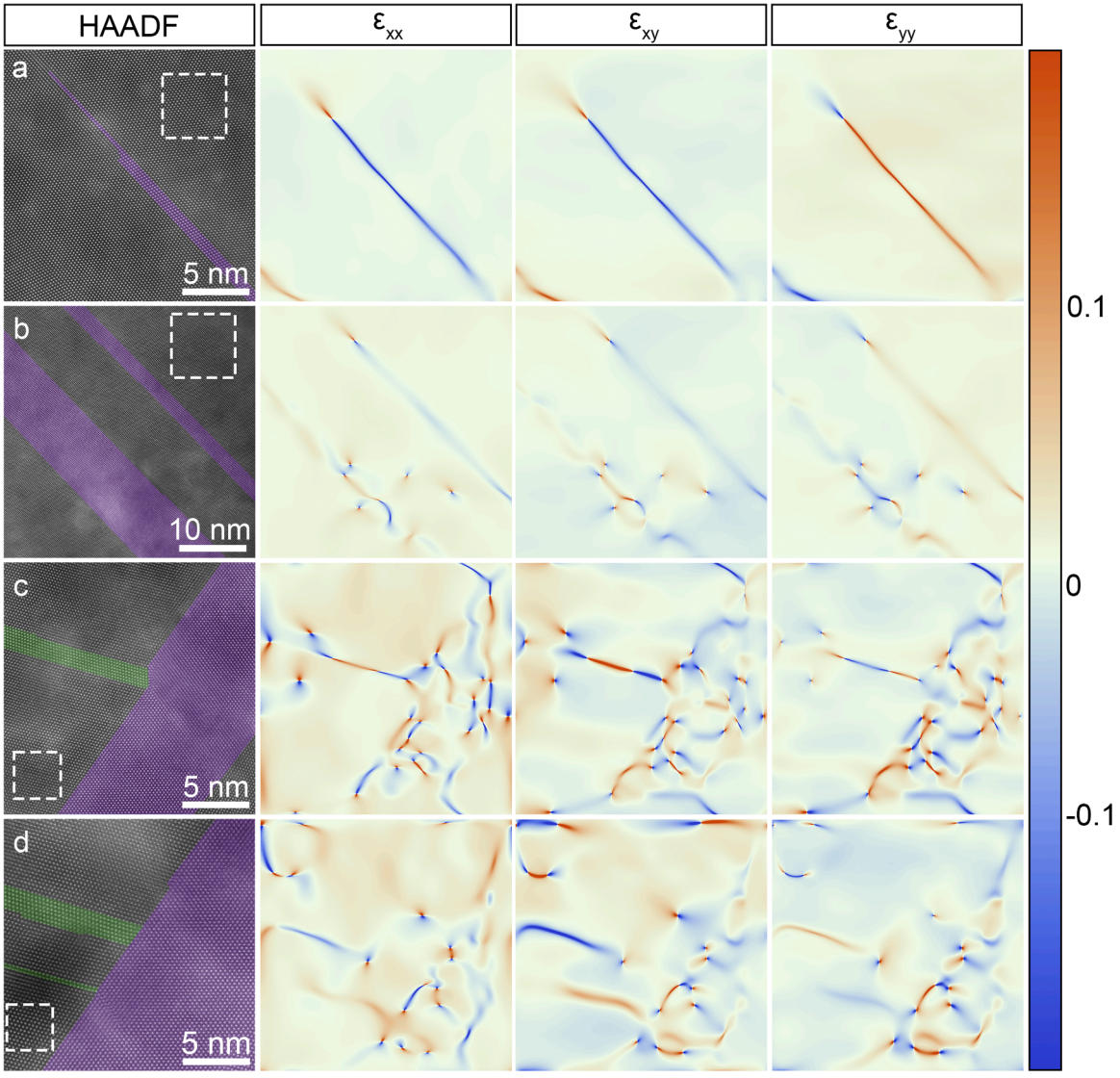

Fig. 12. GPA analysis showing local strain fields around different structures of twins. A STEM-HAADF image is shown for each scenario, with a white square indicating the site used as reference lattices. Corresponding GPA images illustrate the strain field maps of horizontal normal strain (ε_{xx}), shear strain (ε_{xy}), and vertical normal strain (ε_{yy}). (a) A single twin with steps on a TB. (b) Two parallel twins. (c) Two intersecting twins with a step on one of them. (d) Two intersecting twins without steps.

behind this behaviour, geometric phase analysis (GPA) and schematic illustration were utilised, leading to two key conclusions.

First, twin–twin interaction results in significant stress concentration. While such stress concentrations can be accommodated in bulk materials with sufficient strain-hardening capability, they can be fatal in small-sized samples, leading to premature necking. Fig. 12a–12d present local strain fields around four types of twin configurations, as measured by GPA [97]. The local strain of each site is measured relative to a reference site marked by a white square. In the STEM-HAADF images, a set of {111} planes is oriented horizontally, so the measured components ε_{xx}, ε_{yy}, and ε_{xy} represent normal strain on {112} planes, normal strain on {111} planes, and shear strain on {111} planes, respectively. Although these GPA measurements were performed on post-deformation samples (after unloading), the residual lattice distortions still provide a valid qualitative indication of the stress states present during deformation. As shown in Fig. 12a and 12b, only minor lattice distortions are observed near single twins or parallel twins, even in the presence of steps on TBs. In contrast, Fig. 12c and 12d show twin intersections, differing mainly in whether a step forms on one of the TBs. In both cases, GPA reveals pronounced local elastic strain within the thick twin, suggesting the presence of stress concentration. Although this strain does not appear exactly at the intersection point, this behaviour is reasonable. Stress concentrations generated at twin–twin intersections are known to relax during subsequent deformation through mechanisms such as crystal rotation, phase transformations, or dislocation reactions [98,99]. Because GPA analysis was performed on samples that had undergone further deformation after the intersection event, it is expected that the initial stress concentration at the intersection would have been redistributed and transmitted into the adjacent 'barrier' twin, manifesting as dislocation activities and accumulated elastic strain within that region. As a result, when a twin–twin intersection forms, subsequent deformation preferentially localises in this region, driven by the residual stress field, rather than proceeding uniformly through twin nucleation across the sample.

The second reason is that, compared to single twinning, twin–twin interactions accelerate cross-sectional reduction and lead to more severe necking. Fig. 13a and 13b schematically illustrate the structural evolution of a sample subjected to a loading direction aligned with the [110] axis. When twins form along different directions and intersect, they interpenetrate and create two trianglar matrix regions between them (Fig. 13b). As the intersecting twins simultaneously thicken, the matrix between them narrows rapidly, forming a pronounced necked region much thinner than the surrounding areas. Combined with the stress concentration induced by twin–twin interactions, this significantly increases the likelihood of fracture. However, it is worth noting that while the twin–twin interpenetration structure is clearly observed in this study and is known to promote brittle fracture, its formation mechanism remains unclear and warrants further investigation.

In contrast, when the [110] axis is misaligned with the loading direction (Fig. 13c), the necking region typically involves only a single twin (Fig. 13d). As a result, the reduction in cross-sectional area due to twin thickening proceeds more gradually compared to the double twinning scenario. The presence of a single twin would naturally cause a lateral shift between the upper and lower portions of the sample if no external constraints were present. However, during actual tensile testing, the tensile grips constrain both ends of the sample to maintain a uniaxial loading axis, preventing any lateral displacement induced by single twinning. To accommodate these constraints, the twinned regions undergo crystallographic rotation [100,101], allowing the sample to realign along the loading axis, as illustrated in Fig. 13d. This is evidenced by the gradual change in the inclination angles of TBs at different positions along the sample, as displayed in Fig. 13e. Such reorientation helps redistribute strain away from the necking region, suppresses further strain localisation, and ultimately enhances ductility.

4.3. *Effect of different modes of TB motion on mechanical behaviour*

Through quantative in-situ tensile tests, this study observed samples dominated by two different modes of TB motion: TB migration and TB sliding. Twin-boundary migration involves the glide of a single partial dislocation along the TB, resulting in twin thickening [44]. In contrast, TB sliding proceeds through the nucleation and gliding of dissociated full dislocations along the TB [44,45]. In this mechanism, a leading partial transforms an atomic layer of the matrix into a twin, while a trailing partial reverts it back to the matrix. A critical condition for TB sliding is that the Schmid factors of the leading and trailing partial dislocations are comparable [44].

The mode of TB motion has little effect on yield strength, as yielding reflects the onset of plasticity, which is well before TB-mediated processes, such as sliding or migration, become active. Instead, the mode of TB motion primarily influences the ductility. Our results show that stress–strain curves of samples dominated by TB sliding typically exhibit a pronounced strain burst at the onset of TB sliding. This is attributed to the sudden nucleation of a large number of dissociated full dislocations at TB surface steps, where stress concentration occurs, followed by avalanche-like gliding along the TB [102,103]. This is then followed by rapid relative displacement between the matrix and the twin, suggesting that TBs offer little resistance to dislocations gliding on planes parallel to them [104]. The associated localised deformation and stress concentration lead to accelerated necking and severely reduced ductility.

In contrast, samples dominated by TB migration undergo more gradual necking and exhibit slower stress drop, thus maintaining better ductility. However, it is important to note that these conclusions are based on tests in which the loading direction forms an angle of

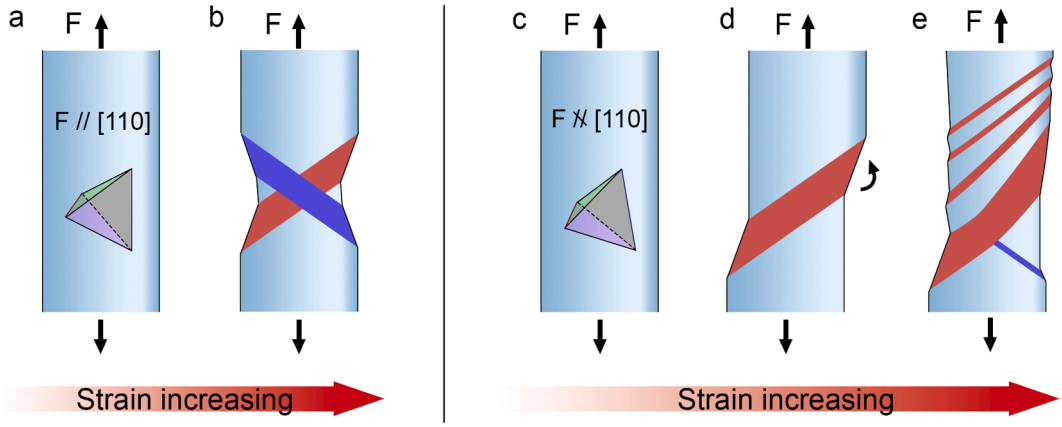

Fig. 13. Schematic illustration of structural evolution of samples subjected to a tensile force that is (a–b) aligned with the [110] axis or (c–e) misaligned with the [110] axis. The red and dark blue areas indicate twins along different directions.

approximately 55° with the twinning plane. Prior studies have shown that the influence of TB sliding on ductility is orientation-dependent; under pure shear loading parallel to the TB, TB-sliding-dominated deformation can still exhibit considerable deformability [45].

In our experiments, TB sliding was most likely facilitated by an out-of-plane deviation of the loading axis from the ideal [110] orientation. This deviation may have arisen from crystal rotation during sample preparation or minor misalignment in the experimental setup. The crystallographic condition is illustrated in Fig. 14, where the Thompson tetrahedron from Fig. 1a is embedded in a unit cell for clarity. Assume that ABC is the active twinning plane, and δ is the centroid of triangle ABC. When the tensile direction is aligned along vector AD (the designed loading condition), the Schmid factors for the leading partials ($C\delta$ or $B\delta$) are 0.236, while that of the trailing partial (δA) is 0.471, favouring TB migration. However, when the loading direction deviates toward DP, the Schmid factors for both ($C\delta$) and (δA) become 0.424, making TB sliding more likely.

Our observations also show that TB sliding is not restricted to a specific alloy composition. Both HEA-LSFE and HEA-HSFE samples exhibited TB sliding when tested under the above-mentioned loading conditions. Together with prior reports of TB sliding in other FCC systems [44,45], this suggests that the activation of TB sliding is governed primarily by the loading geometry rather than by the chemical composition of the alloy.

While TB sliding is commonly observed in small-sized samples [44–46], it is rarely reported in bulk materials. This may be attributed to geometric constraints from surrounding grains [43] and insufficient resolved shear stress to simultaneously activate both partial dislocations [42]. Further studies are needed to confirm the occurrence of TB sliding in bulk materials and to better understand its influence on macroscopic mechanical behaviour.

5. Conclusions

By employing quantitative in-situ tensile straining TEM and various microstructural characterisation techniques, this study investigated how twin density, twin–twin interaction, and TB motion mode influence the mechanical behaviour of small-sized single-crystalline samples. Although size effects inherent to nanoscale systems may lead to certain observations that are not directly transferable to larger-scale materials, the mechanistic insights regarding defect nucleation, interaction, and modes of motion identified in this study remain valid regardless of sample dimensions. The main findings are summarised below:

(1) Reducing the SFE of HEAs through compositional adjustment leads to a higher density of thinner deformation twins. This increased twin density enhances dislocation storage capacity and promotes a more uniform strain distribution, thereby improving the ductility of small-sized samples. However, this ductility-enhancing effect can be easily compromised by severe stress concentration sites, such as twin–twin interpenetration. This suggests that improving ductility in small-scale materials relies more on avoiding stress concentration and maintaining morphological stability than solely increasing dislocation storage capacity. Additionally, the lower SFE reduces the yield strength of single crystals, as it lowers the stress required to initiate partial dislocation slip.

(2) By varying the loading direction relative to the crystal orientation, distinct twinning behaviours were observed. When the loading condition activates two twinning systems with similar Schmid factors, simultaneous twinning on the two twinning systems occurs, often resulting in twin–twin intersections or interpenetrations at early deformation stages. These interactions induce stress concentration and localised necking, promoting premature fracture and reducing ductility. In contrast, when the loading direction favours one twinning system over the other, intense twin–twin interactions are avoided at early stages of deformation. Although stress concentration at twin intersection sites may still lead to eventual failure, the overall ductility is significantly better than in the dual-system case.

(3) When the Schmid factors favour the nucleation and glide of dissociated full dislocations along TBs, TB sliding becomes the dominant deformation mode. Since TBs offer minimal resistance to dislocations gliding on planes parallel to them, TB sliding leads to highly localised deformation and substantial sliding-off between the matrix and the twin. The flow stress required to sustain TB sliding remains lower than that observed in TB-migration-dominated deformation. Consequently, TB sliding substantially reduces the ductility of small-sized samples.

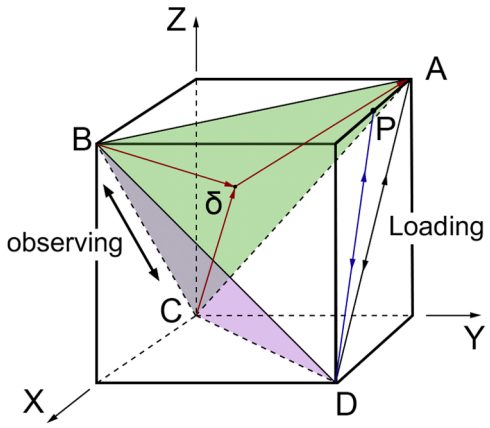

Fig. 14. Schematic of a unit cell of the single-crystalline sample illustrating the loading condition that triggers TB sliding. A Thompson tetrahedron is embedded within the unit cell, with δ denoting the centroid of triangle ABC. The observing direction in TEM lies along BC. The intended tensile loading direction is along AD, while DP represents a potential loading direction resulting from out-of-plane deviation.

CRediT authorship contribution statement

Jinqiao Liu: Writing – original draft, Visualization, Validation, Methodology, Investigation, Formal analysis, Data curation, Conceptualization. **Ranming Niu:** Writing – review & editing, Validation, Methodology, Investigation, Formal analysis, Conceptualization. **Ji Gu:** Methodology, Investigation, Formal analysis. **Ying Liu:** Writing – review & editing, Validation, Investigation, Formal analysis. **Song Ni:** Writing – review & editing, Validation, Formal analysis. **Julie Cairney:** Writing – review & editing. **Min Song:** Writing – review & editing, Supervision. **Yiu-Wing Mai:** Writing – review & editing. **Ting Zhu:** Writing – review & editing. **Xiaozhou Liao:** Writing – review & editing, Validation, Supervision, Resources, Project administration, Methodology, Funding acquisition, Conceptualization.

Declaration of competing interest

The authors declare that they have no known competing financial interests or personal relationships that could have appeared to influence the work reported in this paper.

Acknowledgements

X.L. acknowledges the support from the Australian Research Council [DP230100183 and DP250103207]. The authors are grateful for the scientific and technical support from Sydney Microscopy and Microanalysis (SMM). SMM is a Core Research Facility of the University of Sydney and a foundational node of Microscopy Australia (ROR: 042mm0k03) which is supported by the Australian Government's

National Collaborative Research Infrastructure Scheme.

Supplementary materials

Supplementary material associated with this article can be found, in the online version, at doi:10.1016/j.actamat.2025.121880.

References

[1] C.T. Leondes, MEMS/NEMS Handbook Techniques and Applications, Springer, New York, 2006.
[2] S.S. Ray, J. Bandyopadhyay, Nanotechnology-enabled biomedical engineering: current trends, future scopes, and perspectives, Nanotechnol. Rev. 10 (2021) 728–743, https://doi.org/10.1515/ntrev-2021-0052.
[3] E. Edwards, C. Brantley, P.B. Ruffin, Overview of nanotechnology in military and aerospace applications, in: TO Mensah, B. Wang, G. Bothun, J. Winter, V. Davis (Eds.), Nanotechnology Commercialization, John Wiley & Sons, Inc., Hoboken, 2017, https://doi.org/10.1002/9781119371762.ch5.
[4] J.R. Greer, J.T.M. De Hosson, Plasticity in small-sized metallic systems: intrinsic versus extrinsic size effect, Prog. Mater. Sci. 56 (2011) 654–724, https://doi.org/10.1016/j.pmatsci.2011.01.005.
[5] O. Kraft, P.A. Gruber, R. Mönig, D. Weygand, Plasticity in confined dimensions, Annu. Rev. Mater. Res. 40 (2010) 293–317, https://doi.org/10.1146/annurev-matsci-082908-145409.
[6] Z.W. Shan, R.K. Mishra, S.A. Syed Asif, O.L. Warren, A.M. Minor, Mechanical annealing and source-limited deformation in submicrometre-diameter nicrystals, Nat. Mater. 7 (2008) 115–119, https://doi.org/10.1038/nmat2085.
[7] Z.J. Wang, Q.J. Li, Z.W. Shan, J. Li, J. Sun, E. Ma, Sample size effects on the large strain bursts in submicron aluminum pillars, Appl. Phys. Lett. 100 (2012) 071906, https://doi.org/10.1063/1.3681582.
[8] Y.B. Wang, L.F. Wang, H.J. Joyce, Q. Gao, X.Z. Liao, Y.W. Mai, H.H. Tan, J. Zou, S.P. Ringer, H.J. Gao, C. Jagadish, Super deformability and young's modulus of gaas nanowires, Adv. Mater. 23 (2011) 1356–1360, https://doi.org/10.1002/adma.201004122.
[9] M.D. Uchic, D.M. Dimiduk, J.N. Florando, W.D. Nix, Sample dimensions influence strength and crystal plasticity, Science 305 (2004) 986–989, https://doi.org/10.1126/science.1098993.
[10] W.Z. Han, L. Huang, S. Ogata, H. Kimizuka, Z.C. Yang, C. Weinberger, Q.J. Li, B. Y. Liu, X.X. Zhang, J. Li, E. Ma, Z.W. Shan, From "smaller is stronger" to "size-independent strength plateau": towards measuring the ideal strength of iron, Adv. Mater. 27 (2015) 3385–3390, https://doi.org/10.1002/adma.201500377.
[11] K. Youssef, M. Sakaliyska, H. Bahmanpour, R. Scattergood, C. Koch, Effect of stacking fault energy on mechanical behavior of bulk nanocrystalline Cu and Cu alloys, Acta Mater. 59 (2011) 5758–5764, https://doi.org/10.1016/j.actamat.2011.05.052.
[12] J. Wang, Z. Zeng, C.R. Weinberger, Z. Zhang, T. Zhu, S.X. Mao, In situ atomic-scale observation of twinning-dominated deformation in nanoscale body-centred cubic tungsten, Nat. Mater. 14 (2015) 594–600, https://doi.org/10.1038/nmat4228.
[13] J.W. Christian, S. Mahajan, Deformation twinning, Prog. Mater. Sci. 39 (1995) 1–157, https://doi.org/10.1002/pssb.2221910204.
[14] Y.T. Zhu, X.Z. Liao, X.L. Wu, Deformation twinning in nanocrystalline materials, Prog. Mater. Sci. 57 (2012) 1–62, https://doi.org/10.1016/j.pmatsci.2011.05.001.
[15] Z. You, X. Li, L. Gui, Q. Lu, T. Zhu, H. Gao, L. Lu, Plastic anisotropy and associated deformation mechanisms in nanotwinned metals, Acta Mater. 61 (2013) 217–227, https://doi.org/10.1016/j.actamat.2012.09.052.
[16] L. Wang, K. Du, C. Yang, J. Teng, L. Fu, Y. Guo, Z. Zhang, X. Han, In situ atomic-scale observation of grain size and twin thickness effect limit in twin-structural nanocrystalline platinum, Nat. Commun. 11 (2020) 1167, https://doi.org/10.1038/s41467-020-14876-y.
[17] G. Laplanche, A. Kostka, C. Reinhart, J. Hunfeld, G. Eggeler, E.P. George, Reasons for the superior mechanical properties of medium-entropy CrCoNi compared to high-entropy CrMnFeCoNi, Acta Mater. 128 (2017) 292–303, https://doi.org/10.1016/j.actamat.2017.02.036.
[18] Q. Ding, X. Fu, D. Chen, H. Bei, B. Gludovatz, J. Li, Z. Zhang, E.P. George, Q. Yu, T. Zhu, R.O. Ritchie, Real-time nanoscale observation of deformation mechanisms in CrCoNi-based medium- to high-entropy alloys at cryogenic temperatures, Mater. Today 25 (2019) 21–27, https://doi.org/10.1016/j.mattod.2019.03.001.
[19] O. Bouaziz, Strain-hardening of twinning-induced plasticity steels, Scr. Mater. 66 (2012) 982–985, https://doi.org/10.1016/j.scriptamat.2011.11.029.
[20] S.R. Kalidindi, A.A. Salem, R.D. Doherty, Role of deformation twinning on strain hardening in cubic and hexagonal polycrystalline metals, Adv. Eng. Mater. 5 (2003) 229–232, https://doi.org/10.1002/adem.200300320.
[21] L. Wang, J. Teng, D. Kong, G. Yu, J. Zou, Z. Zhang, X. Han, In situ atomistic deformation mechanisms of twin-structured nanocrystal Pt, Scr. Mater. 147 (2018) 103–107, https://doi.org/10.1016/j.scriptamat.2018.01.012.
[22] A. Gali, E.P. George, Tensile properties of high- and medium-entropy alloys, Intermetallics 39 (2013) 74–78, https://doi.org/10.1016/j.intermet.2013.03.018.
[23] S.F. Liu, Y. Wu, H.T. Wang, W.T. Lin, Y.Y. Shang, J.B. Liu, K. An, X.J. Liu, H. Wang, Z.P. Lu, Transformation-reinforced high-entropy alloys with superior mechanical properties via tailoring stacking fault energy, J. Alloys Compd. 792 (2019) 444–455, https://doi.org/10.1016/j.jallcom.2019.04.035.
[24] Y.H. Zhao, J.F. Bingert, X.Z. Liao, B.Z. Cui, K. Han, A.V. Sergueeva, A. K. Mukherjee, R.Z. Valiev, T.G. Langdon, Y.T. Zhu, Simultaneously increasing the ductility and strength of ultra-fine-grained pure copper, Adv. Mater. 18 (2006) 2949–2953, https://doi.org/10.1002/adma.200601472.
[25] B. Gludovatz, A. Hohenwarter, D. Catoor, E.H. Chang, E.P. George, R.O. Ritchie, A fracture-resistant high-entropy alloy for cryogenic applications, Science 345 (2014) 1153–1158, https://doi.org/10.1126/science.1254581 (1979).
[26] C. Yang, L. Fu, Y. Guo, Y. Ma, D. Li, Z. Wang, Z. Zhang, L. Wang, X. Han, In situ observation of distance dependence of the plasticity behavior of the crack tip in nanosized AuAg alloys, Mater. Charact. 194 (2022) 112432, https://doi.org/10.1016/j.matchar.2022.112432.
[27] K. Ming, X. Bi, J. Wang, Microstructures and deformation mechanisms of Cr26Mn20Fe20Co20Ni14 alloys, Mater. Charact. 134 (2017) 194–201, https://doi.org/10.1016/j.matchar.2017.10.022.
[28] A. Singh, L. Tang, M. Dao, L. Lu, S. Suresh, Fracture toughness and fatigue crack growth characteristics of nanotwinned copper, Acta Mater. 59 (2011) 2437–2446, https://doi.org/10.1016/j.actamat.2010.12.043.
[29] Z. Cheng, H. Zhou, Q. Lu, H. Gao, L. Lu, Extra strengthening and work hardening in gradient nanotwinned metals, Science 362 (2018) eaau1925, https://doi.org/10.1126/science.aau1925.
[30] G. Dehm, Miniaturized single-crystalline fcc metals deformed in tension: new insights in size-dependent plasticity, Prog. Mater. Sci. 54 (2009) 664–688, https://doi.org/10.1016/j.pmatsci.2009.03.005.
[31] F. Mignerot, B. Kedjar, H. Bahsoun, L. Thilly, Size-induced twinning in InSb semiconductor during room temperature deformation, Sci. Rep. 11 (2021) 19441, https://doi.org/10.1038/s41598-021-98492-w.
[32] Q. Zhu, Q. Huang, Y. Tian, S. Zhao, Y. Chen, G. Cao, K. Song, Y. Zhou, W. Yang, Z. Zhang, X. An, H. Zhou, J. Wang, Hierarchical twinning governed by defective twin boundary in metallic materials, Sci. Adv. 8299 (2022) eabn8299.
[33] L. Wang, P. Guan, J. Teng, P. Liu, D. Chen, W. Xie, D. Kong, S. Zhang, T. Zhu, Z. Zhang, E. Ma, M. Chen, X. Han, New twinning route in face-centered cubic nanocrystalline metals, Nat. Commun. 8 (2017) 2142, https://doi.org/10.1038/s41467-017-02393-4.
[34] S. Sun, D. Kong, D. Li, X. Liao, D. Liu, S. Mao, Z. Zhang, L. Wang, X. Han, Atomistic mechanism of stress-induced combined slip and diffusion in sub-5 nanometer-sized Ag nanowires, ACS Nano 13 (2019) 8708–8716, https://doi.org/10.1021/acsnano.9b00474.
[35] Z.Y. Liang, M.X. Huang, Deformation twinning in small-sized face-centred cubic single crystals: experiments and modelling, J. Mech. Phys. Solids 85 (2015) 128–142, https://doi.org/10.1016/j.jmps.2015.09.004.
[36] Z.Y. Liang, J.T.M. De Hosson, M.X. Huang, Size effect on deformation twinning in face-centred cubic single crystals: experiments and modelling, Acta Mater. 129 (2017) 1–10, https://doi.org/10.1016/j.actamat.2017.02.063.
[37] Z.X. Wu, Y.W. Zhang, D.J. Srolovitz, Dislocation-twin interaction mechanisms for ultrahigh strength and ductility in nanotwinned metals, Acta Mater. 57 (2009) 4508–4518, https://doi.org/10.1016/j.actamat.2009.06.015.
[38] L. Lu, Y. Shen, X. Chen, L. Qian, K. Lu, Ultrahigh strength and high electrical conductivity in copper, Science 304 (2004) 422–426, https://doi.org/10.1126/science.1092905.
[39] K. Lu, L. Lu, S. Suresh, Strengthening materials by engineering coherent internal boundaries at the nanoscale, Science 324 (2009) 349–352, https://doi.org/10.1126/science.1159610.
[40] J. Wang, G. Cao, Z. Zhang, F. Sansoz, Size-dependent dislocation-twin interactions, Nanoscale 11 (2019) 12672–12679, https://doi.org/10.1039/c9nr03637g.
[41] L. Wang, Y. Lu, D. Kong, L. Xiao, X. Sha, J. Sun, Z. Zhang, X. Han, Dynamic and atomic-scale understanding of the twin thickness effect on dislocation nucleation and propagation activities by in situ bending of Ni nanowires, Acta Mater. 90 (2015) 194–203, https://doi.org/10.1016/j.actamat.2015.02.002.
[42] Q. Yu, J. Wang, Y. Jiang, R.J. McCabe, N. Li, C.N. Tomé, Twin-twin interactions in magnesium, Acta Mater. 77 (2014) 28–42, https://doi.org/10.1016/j.actamat.2014.05.030.
[43] F. Mokdad, D.L. Chen, D.Y. Li, Twin-twin interactions and contraction twin formation in an extruded magnesium alloy subjected to an alteration of compressive direction, J. Alloys Compd. 737 (2018) 549–560, https://doi.org/10.1016/j.jallcom.2017.12.043.
[44] Z.J. Wang, Q.J. Li, Y. Li, L.C. Huang, L. Lu, M. Dao, J. Li, E. Ma, S. Suresh, Z. W. Shan, Sliding of coherent twin boundaries, Nat. Commun. 8 (2017) 1108, https://doi.org/10.1038/s41467-017-01234-8.
[45] Q. Zhu, L. Kong, H. Lu, Q. Huang, Y. Chen, Y. Liu, W. Yang, Z. Zhang, F. Sansoz, H. Zhou, J. Wang, Revealing extreme twin-boundary shear deformability in metallic nanocrystals, Sci. Adv. 7 (2021) eabe4758, https://doi.org/10.1126/sciadv.abe4758.
[46] L. Wang, J. Teng, Y. Wu, X. Sha, S. Xiang, S. Mao, G. Yu, Z. Zhang, J. Zou, X. Han, In situ atomic scale mechanisms of strain-induced twin boundary shear to high angle grain boundary in nanocrystalline Pt, Ultramicroscopy 195 (2018) 69–73, https://doi.org/10.1016/j.ultramic.2018.08.022.
[47] B.Y. Liu, K.E. Prasad, N. Yang, F. Liu, Z.W. Shan, In-situ quantitative TEM investigation on the dynamic evolution of individual twin boundary in magnesium under cyclic loading, Acta Mater. 179 (2019) 414–423, https://doi.org/10.1016/j.actamat.2019.08.043.
[48] B.Y. Liu, B. Li, Z.W. Shan, Twin boundary migration creating zero shear strain: in-situ TEM observations and atomistic simulations, Magnes. Technol. (2013) 107–111, https://doi.org/10.1007/978-3-319-48150-0_18.

[49] R. Niu, X. An, L. Li, Z. Zhang, Y.W.W. Mai, X. Liao, Mechanical properties and deformation behaviours of submicron-sized Cu–Al single crystals, Acta Mater. 223 (2021) 117460, https://doi.org/10.1016/j.actamat.2021.117460.
[50] Y. Zhang, N.R. Tao, K. Lu, Effect of stacking-fault energy on deformation twin thickness in Cu-Al alloys, Scr. Mater. 60 (2009) 211–213, https://doi.org/10.1016/j.scriptamat.2008.10.005.
[51] A.J. Zaddach, C. Niu, C.C. Koch, D.L. Irving, Mechanical properties and stacking fault energies of NiFeCrCoMn high-entropy alloy, JOM 65 (2013) 1780–1789, https://doi.org/10.1007/s11837-013-0771-4.
[52] A. Rohatgi, K.S. Vecchio, G.T. Gray, The influence of stacking fault energy on the mechanical behavior of Cu and Cu-al alloys: deformation twinning, work hardening, and dynamic recovery, Metall. Mater. Trans. A Phys. Metall. Mater. Sci. 32 (2001) 135–145, https://doi.org/10.1007/s11661-001-0109-7.
[53] K.R. Evans, W.F. Flanagan, Solid-solution strengthening of f.c.c. alloys, Philos. Mag. 18 (1968) 977–983, https://doi.org/10.1080/14786436808227520.
[54] M. Laurent-Brocq, L. Perrière, R. Pirès, F. Prima, P. Vermaut, Y. Champion, From diluted solid solutions to high entropy alloys: on the evolution of properties with composition of multi-components alloys, Mater. Sci. Eng. A 696 (2017) 228–235, https://doi.org/10.1016/j.msea.2017.04.079.
[55] C.R. LaRosa, M. Shih, C. Varvenne, M. Ghazisaeidi, Solid solution strengthening theories of high-entropy alloys, Mater. Charact. 151 (2019) 310–317, https://doi.org/10.1016/j.matchar.2019.02.034.
[56] D.B. Miracle, O.N. Senkov, A critical review of high entropy alloys and related concepts, Acta Mater. 122 (2017) 448–511, https://doi.org/10.1016/j.actamat.2016.08.081.
[57] E.P. George, D. Raabe, R.O. Ritchie, High-entropy alloys, Nat. Rev. Mater. 4 (2019) 515–534, https://doi.org/10.1038/s41578-019-0121-4.
[58] C. Wagner, A. Ferrari, J. Schreuer, J.P. Couzinié, Y. Ikeda, F. Körmann, G. Eggeler, E.P. George, G. Laplanche, Effects of Cr/Ni ratio on physical properties of Cr-Mn-Fe-Co-Ni high-entropy alloys, Acta Mater. 227 (2022) 117693, https://doi.org/10.1016/j.actamat.2022.117693.
[59] M. Shih, J. Miao, M. Mills, M. Ghazisaeidi, Stacking fault energy in concentrated alloys, Nat. Commun. 12 (2021) 3590, https://doi.org/10.1038/s41467-021-23860-z.
[60] S.F. Liu, Y. Wu, H.T. Wang, J.Y. He, J.B. Liu, C.X. Chen, X.J. Liu, H.T. Wang, Z. P. Lu, Stacking fault energy of face-centered-cubic high entropy alloys, Intermetallics 93 (2018) 269–273, https://doi.org/10.1016/j.intermet.2017.10.004.
[61] F. Wu, H.M. Wen, E.J. Lavernia, J. Narayan, Y.T. Zhu, Twin intersection mechanisms in nanocrystalline fcc metals, Mater. Sci. Eng. A 585 (2013) 292–296, https://doi.org/10.1016/j.msea.2013.07.063.
[62] S. Zhao, Q. Zhu, X. An, H. Wei, K. Song, S.X. Mao, J. Wang, In situ atomistic observation of the deformation mechanism of Au nanowires with twin–twin intersection, J. Mater. Sci. Technol. 53 (2020) 118–125, https://doi.org/10.1016/j.jmst.2020.03.044.
[63] C.R. Weinberger, W. Cai, Plasticity of metal nanowires, J. Mater. Chem. 22 (2012) 3277–3292, https://doi.org/10.1039/c2jm13682a.
[64] B.Y. Liu, J. Wang, B. Li, L. Lu, X.Y. Zhang, Z.W. Shan, J. Li, C.L. Jia, J. Sun, E. Ma, Twinning-like lattice reorientation without a crystallographic twinning plane, Nat. Commun. 5 (2014) 3297, https://doi.org/10.1038/ncomms4297.
[65] Z.Y. Liang, M.X. Huang, Effects of crystal orientation on deformation twinning and dislocation slip in single crystal micro-pillars of a twinning-induced plasticity steel, Metall. Mater. Trans. A Phys. Metall. Mater. Sci. 52 (2021) 5235–5242, https://doi.org/10.1007/s11661-021-06460-w.
[66] J.P. McCaffrey, M.W. Phaneuf, L.D. Madsen, Surface damage formation during ion-beam thinning of samples for transmission electron microscopy, Ultramicroscopy 87 (2001) 97–104, https://doi.org/10.1016/S0304-3991(00)00096-6.
[67] N. Thompson, Dislocation nodes in face-centred cubic lattices, Proc. Phys. Soc. Sect. B 66 (1953) 481–492, https://doi.org/10.1088/0370-1301/66/6/304.
[68] Q. Yu, L. Qi, R.K. Mishra, J. Li, A.M. Minor, Reducing deformation anisotropy to achieve ultrahigh strength and ductility in Mg at the nanoscale, Proc. Natl. Acad. Sci. U. S. A. 110 (2013) 13289–13293, https://doi.org/10.1073/pnas.1306371110.
[69] D.G. Xie, R.R. Zhang, Z.Y. Nie, J. Li, E. Ma, J. Li, Z.W. Shan, Deformation mechanism maps for sub-micron sized aluminum, Acta Mater. 188 (2020) 570–578, https://doi.org/10.1016/j.actamat.2020.02.013.
[70] D.M. Dimiduk, C. Woodward, R. LeSar, M.D. Uchic, Scale-free intermittent flow in crystal plasticity, Science 312 (2006) 1188–1190, https://doi.org/10.1126/science.1123889.
[71] J. Schwerdtfeger, E. Nadgorny, F. Madani-Grasset, V. Koutsos, J.R. Blackford, M. Zaiser, Scale-free statistics of plasticity-induced surface steps on KCl single crystals, J. Stat. Mech. Theory Exp. (2007) L04001, https://doi.org/10.1088/1742-5468/2007/04/L04001.
[72] K.Y. Xie, S. Shrestha, Y. Cao, P.J. Felfer, Y. Wang, X. Liao, J.M. Cairney, S. P. Ringer, The effect of pre-existing defects on the strength and deformation behavior of α-Fe nanopillars, Acta Mater. 61 (2013) 439–452, https://doi.org/10.1016/j.actamat.2012.09.022.
[73] Z.W. Shan, R.K. Mishra, S.A. Syed Asif, O.L. Warren, A.M. Minor, Mechanical annealing and source-limited deformation in submicrometre-diameter Ni crystals, Nat. Mater. 7 (2008) 115–119, https://doi.org/10.1038/nmat2085.
[74] D. Kiener, A.M. Minor, Source truncation and exhaustion: insights from quantitative in situ TEM tensile testing, Nano Lett. 11 (2011) 3816–3820, https://doi.org/10.1021/nl201890s.
[75] C. Chisholm, H. Bei, M.B. Lowry, J. Oh, S.A. Syed Asif, O.L. Warren, Z.W. Shan, E. P. George, A.M. Minor, Dislocation starvation and exhaustion hardening in Mo alloy nanofibers, Acta Mater. 60 (2012) 2258–2264, https://doi.org/10.1016/j.actamat.2011.12.027.
[76] L. Tian, Z.W. Shan, E. Ma, Ductile necking behavior of nanoscale metallic glasses under uniaxial tension at room temperature, Acta Mater. 61 (2013) 4823–4830, https://doi.org/10.1016/j.actamat.2013.05.001.
[77] W.D. Callister, D.G. Rethwisch, Materials Science and Engineering: An Introduction, John Wiley & Sons, Inc., New York, 2018, https://doi.org/10.1088/0031-9120/5/2/304.
[78] Y.B. Wang, X.Z. Liao, Y.H. Zhao, E.J. Lavernia, S.P. Ringer, Z. Horita, T. G. Langdon, Y.T. Zhu, The role of stacking faults and twin boundaries in grain refinement of a Cu-Zn alloy processed by high-pressure torsion, Mater. Sci. Eng. A 527 (2010) 4959–4966, https://doi.org/10.1016/j.msea.2010.04.036.
[79] J. Narayan, Y.T. Zhu, Self-thickening, cross-slip deformation twinning model, Appl. Phys. Lett. 92 (2008) 151908, https://doi.org/10.1063/1.2911735.
[80] A. Jarlöv, W. Ji, Z. Zhu, Y. Tian, R. Babicheva, R. An, H.L. Seet, M.L.S. Nai, K. Zhou, Molecular dynamics study on the strengthening mechanisms of Cr–Fe–Co–Ni high-entropy alloys based on the generalized stacking fault energy, J. Alloys Compd. 905 (2022) 164137, https://doi.org/10.1016/j.jallcom.2022.164137.
[81] L. Zhang, K. Qian, J. Huang, M. Liu, Y. Shibuta, Molecular dynamics simulation and machine learning of mechanical response in non-equiatomic FeCrNiCoMn high-entropy alloy, J. Mater. Res. Technol. 13 (2021) 2043–2054, https://doi.org/10.1016/j.jmrt.2021.06.021.
[82] Q. Ding, Y. Zhang, X. Chen, X. Fu, D. Chen, S. Chen, L. Gu, F. Wei, H. Bei, Y. Gao, M. Wen, J. Li, Z. Zhang, T. Zhu, R.O. Ritchie, Q. Yu, Tuning element distribution, structure and properties by composition in high-entropy alloys, Nature 574 (2019) 223–227, https://doi.org/10.1038/s41586-019-1617-1.
[83] H. Li, H. Zong, S. Li, S. Jin, Y. Chen, M.J. Cabral, B. Chen, Q. Huang, Y. Chen, Y. Ren, K. Yu, S. Han, X. Ding, G. Sha, J. Lian, X. Liao, E. Ma, J. Sun, Uniting tensile ductility with ultrahigh strength via composition undulation, Nature 604 (2022) 273–279, https://doi.org/10.1038/s41586-022-04459-w.
[84] Q.J. Li, H. Sheng, E. Ma, Strengthening in multi-principal element alloys with local-chemical-order roughened dislocation pathways, Nat. Commun. 10 (2019) 3563, https://doi.org/10.1038/s41467-019-11464-7.
[85] A. Jarlöv, W. Ji, R. Babicheva, Y. Tian, Z. Hu, H.L. Seet, L. Tan, F. Liu, Y. Liu, M.L. S. Nai, U. Ramamurty, K. Zhou, Tailoring short-range order and dislocation evolution in Cr–Co–Ni medium-entropy alloys: a molecular dynamics study, Mater. Des. 240 (2024) 112840, https://doi.org/10.1016/j.matdes.2024.112840.
[86] P. Zhou, Z.Y. Liang, R.D. Liu, M.X. Huang, Evolution of dislocations and twins in a strong and ductile nanotwinned steel, Acta Mater. 111 (2016) 96–107, https://doi.org/10.1016/j.actamat.2016.03.057.
[87] S. Ma, L. Fu, A. Shan, Enhancing strength-ductility of the aluminum bronze alloy by generating high-density ultrafine annealing twins, Mater. Charact. 177 (2021) 111057, https://doi.org/10.1016/j.matchar.2021.111057.
[88] F. Zhao, T. Suo, B. Chen, Y.L. Li, Strength–ductility combination of fine-grained magnesium alloy with high deformation twin density, J. Alloys Compd. 798 (2019) 350–359, https://doi.org/10.1016/j.jallcom.2019.05.260.
[89] O. Bouaziz, N. Guelton, Modelling of TWIP effect on work-hardening, Mater. Sci. Eng. A 319–321 (2001) 246–249, https://doi.org/10.1016/S0921-5093(00)02019-0.
[90] G. Dirras, D. Tingaud, D. Ueda, A. Hocini, K. Ameyama, Dynamic Hall-Petch versus grain-size gradient effects on the mechanical behavior under simple shear loading of β-titanium Ti-25Nb-25Zr alloys, Mater. Lett. 206 (2017) 214–216, https://doi.org/10.1016/j.matlet.2017.07.027.
[91] W. Xu, L.P. Dávila, Tensile nanomechanics and the Hall-Petch effect in nanocrystalline aluminium, Mater. Sci. Eng. A 710 (2018) 413–418, https://doi.org/10.1016/j.msea.2017.10.021.
[92] J.Y. Zhang, Q.F. He, J. Li, Y. Yang, Chemical fluctuation enabling strength-plasticity synergy in metastable single-phase high entropy alloy film with gigapascal yield strength, Int. J. Plast. 139 (2021) 102951, https://doi.org/10.1016/j.ijplas.2021.102951.
[93] L. Li, N.M. Ghoniem, Twin-size effects on the deformation of nanotwinned copper, Phys. Rev. B Condens. Matter Mater. Phys. 79 (2009) 075444, https://doi.org/10.1103/PhysRevB.79.075444.
[94] H. Hu, T. Fu, C. Li, S. Weng, Y. Zhao, X. Chen, X. Peng, Delay of inverse Hall-Petch relationship of nanocrystalline Cu by modifying grain boundaries with coherent twins, Phys. Rev. B 105 (2022) 024107, https://doi.org/10.1103/PhysRevB.105.024107.
[95] S.H. Wang, Z.Y. Liu, G.D. Wang, J.L. Liu, G.F. Liang, Q.L. Li, Effects of twin-dislocation and twin-twin interactions on the strain hardening behavior of TWIP steels, J. Iron Steel Res. Int. 17 (2010) 70–74, https://doi.org/10.1016/S1006-706X(10)60200-2.
[96] D. Shi, T. Liu, D. Hou, H. Chen, F. Pan, H. Chen, The effect of twin-twin interaction in Mg-3Al-1Zn alloy during compression, J. Alloys Compd. 685 (2016) 428–435, https://doi.org/10.1016/j.jallcom.2016.05.338.
[97] M.J. Hÿtch, E. Snoeck, R. Kilaas, Quantitative measurement of displacement and strain fields from HREM micrographs, Ultramicroscopy 74 (1998) 131–146, https://doi.org/10.1016/S0304-3991(98)00035-7.
[98] J. Chen, S. Lu, Z. yong Hou, W. wen Song, Z. yu Liu, G. dong Wang, T. Furuhara, Atomic-scale understanding of twin intersection rotation and ε-martensite transformation in a high Mn twinning-induced plasticity steel, Acta Mater. 271 (2024) 119832, https://doi.org/10.1016/j.actamat.2024.119832.
[99] C.L. Chen, W. Lu, Y.Y. Cui, L.L. He, H.Q. Ye, TEM observations of twin intersections in a Ti-47Al-2Cr-2Nb-0.1Y alloy compressed at room temperature, J. Alloys Compd. 454 (2008) 201–205, https://doi.org/10.1016/j.jallcom.2006.12.127.

[100] D. Kiener, C. Motz, G. Dehm, Dislocation-induced crystal rotations in micro-compressed single crystal copper columns, J. Mater. Sci. 43 (2008) 2503–2506, https://doi.org/10.1007/s10853-008-2531-3.
[101] Q. Wang, J. Wang, J. Li, Z. Zhang, S.X. Mao, Consecutive crystallographic reorientations and superplasticity in body-centered cubic niobium nanowires, Sci. Adv. 4 (2018) eaas8850, https://doi.org/10.1126/sciadv.aas8850.
[102] T. Zhu, J. Li, Ultra-strength materials, Prog. Mater. Sci. 55 (2010) 710–757, https://doi.org/10.1016/j.pmatsci.2010.04.001.
[103] F.F. Csikor, C. Motz, D. Weygand, M. Zaiser, S. Zapperi, Dislocation avalanches, strain bursts, and the problem of plastic forming at the micrometer scale, Science 318 (2007) 251–254, https://doi.org/10.1126/science.1143719.
[104] P.J. Imrich, C. Kirchlechner, G. Dehm, Influence of inclined twin boundaries on the deformation behavior of Cu micropillars, Mater. Sci. Eng. A 642 (2015) 65–70, https://doi.org/10.1016/j.msea.2015.06.064.